Petrological Constrains on Magma Evolution of the Fuji Volcano: A Case Study for the 1707 Hoei Eruption

Takashi Sano[1], Takaaki Fukuoka[2] and Mitsunori Ishimoto[3]

[1] Department of Geology and Paleontology, National Museum of Nature and Science,
3–23–1 Hyakunin-cho, Shinjuku-ku, Tokyo 169–0073, Japan
E-mail: sano@kahaku.go.jp

[2] Faculty of Geo-environmental Science, Rissho University, 1700 Magechi, Kumagaya-shi, Saitama 360–0914, Japan

[3] Nuclear Professional School, School of Engineering, The University of Tokyo,
2–4 Shirakatashirane, Tokai-mura, Naka-gun, Ibaraki 319–1195, Japan

Abstract.　In order to examine magma evolution of the Fuji volcano, we have reported porosity, petrography, mineral compositions, and whole rock compositions of volcanic rocks from 1707 AD eruption. The volcanic rocks are juvenile clasts (scoria and pumice) with compositions of basalt, andesite, and dacite; and lithic fragments with basaltic composition. Phenocryst mode of the volcanic rocks is generally low (≤ 3 vol. %), but some andesite clasts and all lithic fragments have relatively high amounts of phenocrysts (up to 15 vol. %). Chemical variations from juvenile basalt to andesite can be explained by fractionation of phenocryst phases from a basaltic magma at nearly dry conditions. On the other hand, a presence of hornblende phenocryst in dacite clasts and similar contents of B and Y in both andesite and dacite clasts suggest that fractional crystallization from andesite to dacite would take place at wet conditions. In addition to the fractional crystallization process, an effect of crustal contamination could be introduced to explain relatively high content of Th in dacite clasts. As for lithic fragments, their magma source is most likely different from that of juvenile clasts because of their low Rb/Y and K_2O/Y ratio and low concentrations of most incompatible elements (Ti, Na, K, P, Rb, Ba, Nb. Pb, Zr, REEs).
Key words:　Fuji volcano, Hoei eruption, scoria, pumice, lithic fragment, hornblende, fractional crystallization, magma chamber.

Introduction

Mt. Fuji is the largest stratovolcano and the highest mountain in Japan. The Fuji volcano is presumably the most famous mountain in Japan because of its beauty and perfect symmetry. It rises to a height of 3776 m (the highest point on Japan) above sea level and has a base diameter of about 50 km. Although Fuji volcano is dormant at present, it is an active volcano and has a number of historical eruptions (at least 10 eruptions; Koyama, 1998). Since Fuji volcano has a large eruption rate of magma than most other Japanese stratovolcanoes by one order of magnitude (Fujii, 2001), a large amount of magma would fill a magma chamber beneath the volcano. When the magma chamber is filled with the magma, next

eruption would take place. We should consider the next eruption now, because Fuji volcano has not erupted about 300 years since the most recent eruption, which is called Hoei eruption, in 1707 AD.

One of the most important basic studies to predict the next eruption is to understand magma chamber processes. The first step is to examine magma evolution processes such as fractional crystallization, magma mixing, crustal contamination, and so on. Since almost of all volcanic rocks from Fuji volcano have only basaltic compositions (e.g., Takahashi *et al*., 2003), they would not be used to examine the magma evolution processes producing wide compositional range. On the other hand, volcanic ejecta of Hoei eruption are good samples because they are vari-

ous rocks ranging from basalt to dacite (Tsuya, 1955; Miyaji, 1984). Previous studies suggested that a compositionally zoned magma chamber was present beneath the Fuji volcano before the Hoei eruption (Koyaguchi, 1986; Togashi *et al.*, 1991, 2007; Watanabe *et al.*, 2006), because the volcanic ejecta have the wide compositional variation. On the basis of mineralogical, whole rock, and Nd-Sr-Pb isotope compositions, Watanabe *et al.* (2006) have proposed that crystal fractionation played a major role in the development of chemical zonation in the magma chamber. They also suggested that Os isotope ratio shows an effect of small amounts of crustal contamination in andesite and dacite. In this study, we evaluate the fractional crystallization and crustal contamination processes by using a new data set that has not been evaluated by the previous study (including porosity, detail petrography, mineral compositions, and Cs, Rb, Pb, Y, Th contents in whole rocks).

Geological Background and Samples

Fuji volcano is located on southern edge of the "Fossa Magna", a tectonic zone traversing the central part of the Japan main island (Honshu) from Japan Sea to Pacific Ocean in a NNW-SSE direction (Fig. 1). The southern area of the Fossa Magna, which called South Fossa Magna, is situated at the complex focus of collision because here is a triple junction of Philippine Sea, Pacific, and Eurasian plates. Beneath the South Fossa Magna, Philippine Sea plate penetrates under Eurasian plate and Pacific plate is subducted under the Philippine Sea plate, indicating that two oceanic plates exist beneath Fuji volcano.

The three dimensional structures of the P and S velocities have proposed that a zone of basaltic melts are present at depths of 15–25 km beneath Fuji volcano (Nakamichi *et al.*, 2007). The depths of the zone of basaltic melts, which may be called a magma chamber, corresponds to a location of deep low frequency earthquake (Ukawa, 2005), and depths of a conductive body that estimated from a magnetotelluric survey (Aizawa *et al.*,

2004). When we compare these data to an estimated depth (~10 km) of the upper surface of Philippine Sea plate beneath Fuji volcano (Ishida, 1992), we can conclude that the magma chamber exists within the Philippine Sea plate (Nakamichi *et al.*, 2007).

The magma chamber has provided main magma that produced main body of Fuji volcano. The main body of Fuji volcano is composed of two volcanoes, Older Fuji and Younger Fuji, both of which have been erupted above an older volcano, which is called Komitake volcano (Tsuya, 1940). The first eruption of Older Fuji volcano is estimated to be about 100,000 years ago (Tsuya, 1968, 1971; Machida, 2007), and the last activity of Older Fuji volcano is defined by big collapses of the main body generating a large amounts of debris flow deposits on several areas around Fuji volcano. Sedimentation age of the last debris flow deposit, which called Tanuki debris flow deposit, is estimated to be around 20,000 years ago (Yamamoto *et al.*, 2007). Eruption of Younger Fuji volcano began from effusion of a large amount of basaltic lava flows to several directions of Fuji volcano except for east flank (Tsuya, 1968, 1971; Miyaji, 1988, 2007). After the first eruption of Younger Fuji volcano, hundreds of eruptions have formed the highest stratovolcano in Japan.

The Hoei eruption, the most recent eruption, began with Plinian eruption that explored dacite pumice in the morning (~10 a.m.) of December 16, 1707, and continued until that evening (~4 p.m.). At that evening, eruption materials were changed from dacite pumice to andesite scoria, which erupted until next morning (December 17). After the December 17 morning, scoria clasts with basaltic compositions were jetting by Strombolian-type to subplinian eruptions. On December 25, 1707, a much greater volume subplinian basaltic eruption began and lasted until January 1, 1708 (Miyaji and Koyama, 2007).

During the Hoei eruption, three large craters were formed at the southeast flank of the volcano; Hoei 1st, 2nd, and 3rd craters, arranging from the summit to downslope direction. The arranging direction is the same with NW-SE trending of many
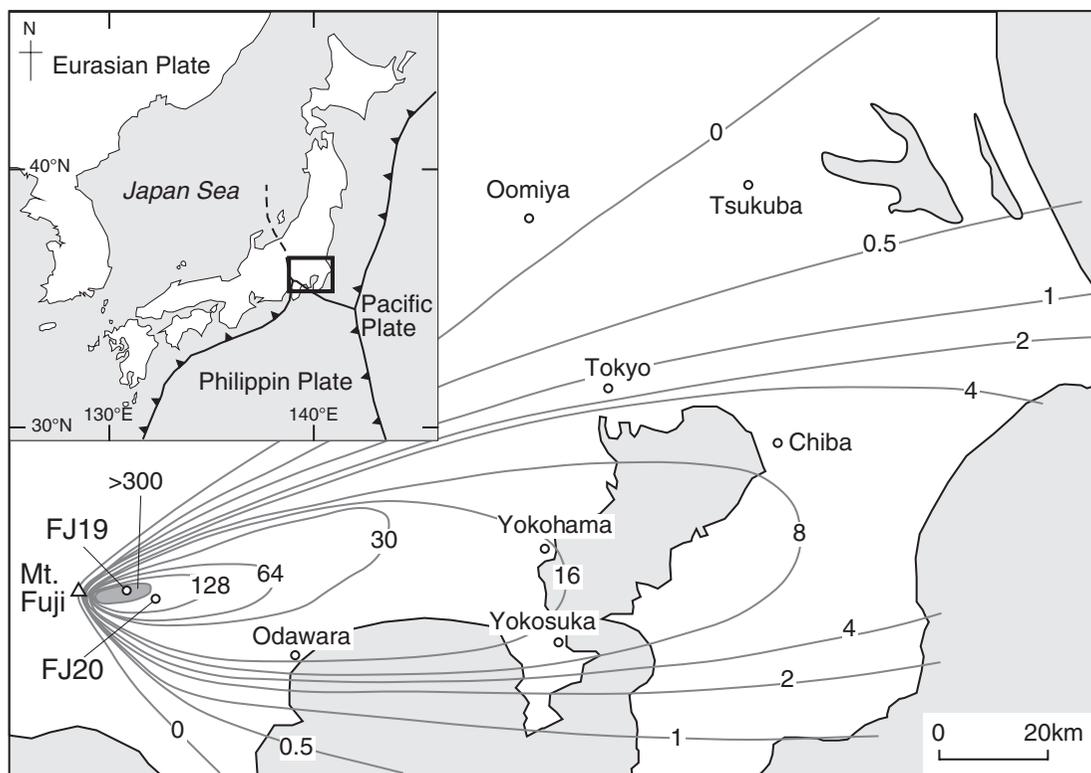
Fig. 1. Map of Mt. Fuji showing the extent of Hoei air-fall deposits, in terms of isopachs (after Miyaji, 1984 and Miyaji and Koyama, 2007), with locations of sampling section (FJ19 and FJ20). The isopach giving thickness in cm. The insert shows tectonic setting and the location of the main map (box).

flank craters on Fuji volcano (Tsuya, 1968, 1971; Takada *et al*., 2007). The 2nd and 3rd craters were the first to open up and explored dacite pumice and andesite scoria. Accessory lithic fragments, which consist of dense basalt, obsidian, and gabbro, were also exploded simultaneously (Tsuya, 1955). The 1st crater was formed after the activity of 2nd and 3rd craters had ceased, and it erupted basalt scoria. The ejecta were dispersed eastward and the thickness of the air-fall deposits exceed three meters at FJ19 section 8 km from the craters and reached a few centimeters even at Edo (present Tokyo), 100 km from Fuji volcano (Fig. 1).

The Hoei air-fall deposits are divided into four major fall units; Ho-I to Ho-IV in ascending order based on differences of porosity and constituents (Fig. 2; Miyaji, 1984). Ho-I is composed of dacite pumice that exploded from the Hoei 2nd and 3rd craters. This unit is subdivided into two units (Ho-Ia and -Ib) on the basis of main constitute clasts; lower Ho-Ia consists of white to brown pumice, and upper Ho-Ib mainly contains dark brown pumice and banded pumice (Miyaji, 1984). Volumetric ratios of dark brown pumice and banded pumice to the white pumice increase toward the upper portion, and therefore, we further subdivided Ho-Ia into two subunits: FJ19-A and FJ19-B (Fig. 2). FJ19-C in this study corresponds to Ho-Ib of Miyaji (1984). A little amount of lithic fragments is also identified in the Unit I. Ho-II consists of black to dark-gray dense scoria with andesitic composition. In addition, several lithic fragments with basaltic compositions and rare dacite pumice are present in the unit. The Ho-II air-fall deposits were also exploded from Hoei 2nd and 3rd craters. On the basis of differences of amount of the constituents and phenocryst abun-
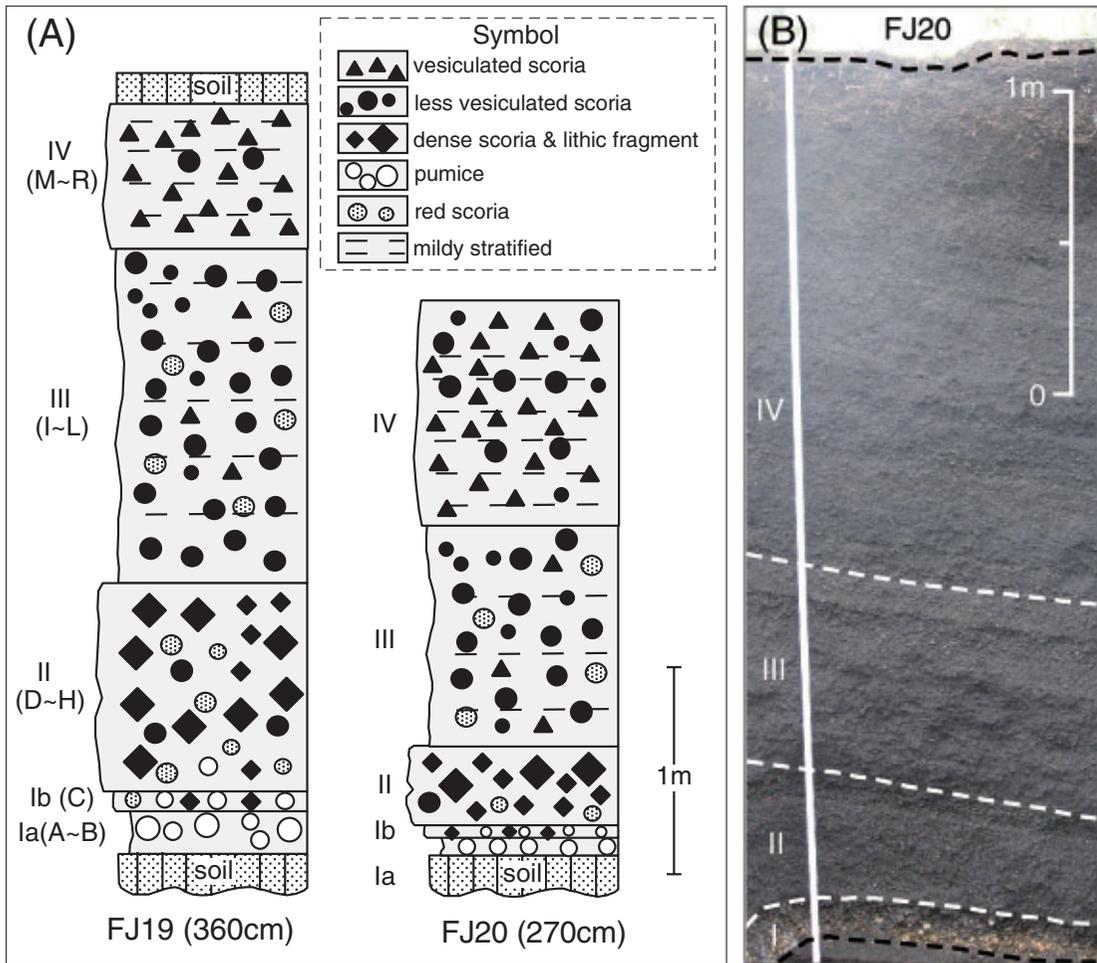
Fig. 2. (A) Columnar sections of sampling sections, and (B) a photograph of a sampling section. Stratigraphic division follows Miyaji (1984). Alphabet in parenthesis indicates subunit defined in this study. Note that samples from FJ20 section were not used in this study.

dances, we subdivided Ho-II into five subunits: FJ19-D to FJ19-H. A remarkable feature of FJ19-D is that it contains some dacite pumice clasts, but other Ho-II subunits have little amounts of them. FJ19-E consists of the dense scoria, and FJ19-F is mainly composed of the lithic fragments. Main constituents of both FJ19-G and FJ19-H are the dense scoria, but phenocryst abundances of FJ19-H are distinctly higher than those of FJ19-G (see Petrography in Results). Ho-III and IV air-fall deposits are basalt scoria that explored from the Hoei 1st crater. Ho-III is alteration of coarse- and fine-grained less vesiculated scoria. Each alteration layer in this unit corresponds to subunits FJ19-I to FJ19-L in this study (Fig. 2). Ho-IV is mildly stratified layers consisting of well-sorted vesiculated scoria. This unit is subdivided into 5 subunits; FJ19-N to FJ19-Q (Fig. 2). Red scoria clasts are generally present in the lower three units (I to III), but their amount is little in Unit IV (Fig. 2).

At the end of the subplinian eruption of Ho-IV scoria, less explosive magma would construct a scoria cone at the bottom of the Hoei 1st crater. One sample (FJ55) was collected from the scoria cone so as to know petrological and geochemical

information of the final eruption material.

During the Hoei eruption, eastern edges of the Hoei 1st and 2nd craters were uplift and Mt. Hoei (Hoei-san) was appeared. The Hoei-san was produced by upheaving of the body of Older Fuji volcano caused by magma instruction during the 1707 eruption (Tsuya, 1968).

Analytical Method

Each data point of most previous studies for the Hoei air-fall deposits was produced by analyses of more than one clast that sampled from the same interval (Miyaji, 1984; Nakamura *et al*., 1986; Watanabe *et al*., 2006). This analytical method is good to know an average composition of each interval. However, heterogeneity of each interval cannot be seen by this method. One important aim of this study is to identify heterogeneity of each subunit of the Hoei air fall deposits. We therefore selected only single homogeneous clast for each analysis. The selection method is very similar to that of Koyaguchi (1986) and Yoshimoto *et al*. (2004). If heterogeneous structures (banded pumice, mixture of mingled magma, and so on) in a single clast were identified by thin section description, we did not conduct further chemical analysis for the sample. Several homogeneous clasts were picked up from each interval of the 17 subunits (A to Q) at the FJ19 site (Figs. 1 and 2).

Since sample volume of each clast was limited (down to 1 cm^3), we firstly conducted non-destructive apparent density measurement. The density was determined by a glass-beads method proposed by Sasaki and Katsui (1981); to determine volume of a clast, it was dropped into graduated cylinder that glass beads entered, and increasing volume was the amount of space the clast took up. When we determined weight of the clast after the volume measurement, the apparent density was calculated. The measurement for each clast was conducted three times and average density and standard deviation were calculated.

After the apparent density measurement, the clast was cut to make a thin section. Petrography of juvenile clasts and lithic fragments is based on 57 thin sections from all units of Hoei eruption (samples in Table 1 and FJ19-D2, -F3, -F4, -R2 rocks). Mineral composition of one hornblende phenocryst in subunit FJ19-C was determined by a scanning electron microscope with link energy dispersive X-ray spectrometer system (SEM-EDS) at National Museum of Nature and Science.

When homogeneity of the clast was confirmed by the petrological description, then the clast was broken in an iron mortar and sieved to millimeter-size chips. Only fresh chips were handpicked and washed ultrasonically, twice in alcohol and twice in distilled water. The cleaned chips were dried for >12 hours in an oven at 110 °C and then grounded to powder in an agate mill.

When the powder had plenty volume (>2 cm^2), a true density was determined by Beckman air compression pycnometer (Tokyo Science Co. Ltd., Model 1000). In order to calculate average density and standard deviation, the measurement was conducted three times as well as that of apparent density. When both apparent and true densities were determined for a clast, its porosity was calculated. After the density measurements and petrological descriptions, whole-rock compositions for the rock powders were determined by three different methods: X-ray fluorescence (XRF) analysis; instrumental neutron activation analysis (INAA); and prompt gamma neutron activation analysis (PGNA).

Analyses of major and selected trace elements of 53 samples were carried out by X-ray fluorescence (XRF) analysis at two laboratories; one is Fuji Tokoha University by using a Rigaku RIX2100 instrument, and another is National Museum of Nature and Science by using a Rigaku RIX1000 instrument.

For the XRF analysis at Fuji Tokoha University, glass beads were prepared from the powders, using anhydrous lithium tetraborate ($Li_2B_4O_7$) as a flux. Each sample powder was mixed with the $Li_2B_4O_7$ flux in the proportion of 1 to 5, and then fused at 1100 °C in a $Pt_{95}Au_5$ crucible and cast into a glass bead. Details of the analytical procedures are given in Sano (2002).

Table 1. Counting condition of each element for XRF analysis.

Element	X-ray Line	Crystal	Angle (2ϑ)			Counting time (s)		Counter	PHA (kV)	Interfere element
			Peak	BG (low)	BG (high)	Peak	BG			
Fe	Kα	LIF1	57.50			40		SC	100-330	
Ti	Kα	LIF1	86.14	85.0	87.0	100	50	SC	100-350	
Rb	Kα	LIF1	26.60	26.0	27.3	200	100	SC	100-300	
Ba	Lα	LIF1	87.14	84.8	88.0	500	250	SC	100-300	Ti
Nb	Kα	LIF1	21.36	21.0	21.8	200	100	SC	100-300	Y
Pb	Lβ1	LIF1	28.24	27.8	28.6	200	100	SC	100-280	
Sr	Kα	LIF1	25.14	24.5	25.7	100	50	SC	100-300	
Y	Kα	LIF1	23.79	23.2	24.4	100	50	SC	100-300	Rb
Zr	Kα	LIF1	22.54	22.0	23.1	100	50	SC	100-300	Sr
Ce	Lβ1	LIF1	71.60	71.0	73.0	500	250	SC	100-300	Zr
Cr	Kα	LIF1	69.33	68.5	70.2	200	100	SC	100-300	V
Ni	Kα	LIF1	48.65	48.0	49.3	100	50	SC	100-300	
Co	Kα	LIF1	52.78	50.45	54.0	200	100	SC	100-310	Fe
V	Kα	LIF1	76.91	76.0	78.0	100	50	SC	100-300	
Th	Lα	LIF1	27.46	27.1	27.8	200	100	SC	100-290	
Zn	Kα	LIF1	41.78	41.1	42.5	200	100	SC	100-300	
S	Kα	Ge	110.82	109.0	113.0	100	50	PC	150-300	

Note: Fe and Ti were analyzed only for purpose to reduce peak overlaps
Abbreviations: BG, background, SC, scintillation counter; PC, proportional counter.

Procedures of XRF analysis at National Museum of Nature and Science were different from those at Fuji Tokoha University. Before the major element analysis, 0.4000 ± 0.0004 g of powder was weighted on a Metler Toledo dual balance system and ignited at 1025 °C for 4 hours in an electric muffle furnace to determine weight loss on ignition (LOI). Replicated analysis of several samples shows that uncertainty on LOI is 0.03 wt %. After determination of LOI, glass beads containing lithium tetraborate flux (10 to 1 dilution of sample) were prepared. For trace elements (Rb, Ba, Nb, Pb, Sr, Zr, Y, Ce, Cr, Ni, Co, V, Th, Zn, S), 4.0–5.0 g of powder was pressed into a pellet by a 12 ton force from a hydraulic press.

For the processing calibration lines of major and trace elements, 15 standard sample of Geological Survey of Japan (GSJ) (JB-1, JB-2, JB-3, JA-1, JA-2, JA-3, JR-2, JR-3, JG-1, JG-2, JG-3, JGb-1, JP-1, JF-1, and JF-2 from Imai *et al.*, 1995), 11 standard samples of the Geological Institute of University of Tokyo (IK437, IK218, IK507, IK565, IK790, IK686, IK332, IK625, IK502 from Yoshida and Takahashi, 1997), 6 standard samples of Korea Institute of Energy and Resources (KB-1, KD-1, KGB-1, KT-1, KG-1, KG-2 from Kimura and Yamada, 1996), one sample of U.S. Geological Survey (RGM-1), and one sample of U.S. Department of Commerce, National Institute of Standard and Technology (278 Obsidian Rock) were used. The XRF technique used are essentially similar to those described by Sano (2002), except for that analytical conditions for the determination of trace elements were different. The analytical conditions are shown in Table 1. The X ray-tube of Rh was fitted in the spectrometer, and accelerating voltage and tube current were set at 50 kV and 50 mA, respectively. In order to improve precision in the determination of trace elements, long counting times (up to 500 s at the peak and 500 s in total at the background positions) were used (Table 1). For trace element analysis, peak overlaps from coexisting elements are a problem (i.e., overlaps of TiKα peak on BaLα, YKβ peak on NbKα, RbKβ peak on YKα, SrKβ peak on ZrKα, and so on; see interfere element in Table 1). The peak overlaps were reduced by the following equation (a computer program in the RIX1000 system): $W_i = bI_i + c + I_jW_j$, where, W_i is weight percent of analytical

element, W_j is weight percent of interfere element, I_i is intensity of analytical element, I_j is intensity of interfere element, and b and c are constant correction factors. The correction factors were calculated by regressions of the standard samples. Replicate analysis of GSJ standard JB-1a (this sample was not used for the standard to make calibration lines) and one sigma of standard deviation of each calibration line indicate overall precision and accuracy (Table 2). Accuracy of the XRF was also checked by comparison of the XRF data produced by two different laboratories because 7 samples (FJ19-F1, -H1, -H3, -J1, -L1, -O1 and -R1) were analyzed twice, one was at National Museum of Nature and Science and another was at Fuji Tokoha University (Table 2). The comparisons show that there are good agreements between the data that produced by the two laboratories. The differences are within one sigma of standard deviation of each calibration line (Table 2).

A non-destructive INAA technique was used for the analysis of Cs, Th, Hf, Cr, and rare-earth elements (REE; La, Ce, Nd, Sm, Eu, Tb, Yb, and Lu) on 30 samples (Table 2). The powders (0.6–0.9 g) were activated with thermal neutrons for 6 hours with 4.5×10^{13} n/cm^2·s at the 'TB pipe' of JRR-4 reactor of Japan Atomic Energy Agency (JAEA). Simultaneously, JB-1, JB-3, and JR-2 were activated as standards. After suitable times (one week and one month), the gamma spectra of activated samples were counted by Ge detector coupled to a 2048 multi-channel analyzer at the Inter-University Laboratory for the Common Use of Nuclear Facilities, the University of Tokyo. The details of the analytical procedures have been described by Fukuoka et al. (1987). The analytical error involved in the results is $< \pm 5$ % (Table 2).

Boron, Ti, K, Gd, and Sm contents of 27 samples were determined by PGNA at the thermal neutron beam guide of the JRR-3M reactor, JAEA (Yonezawa, 1993). The powders (0.6–1.0 g) were cold presses into disks (12 mm in diameter and 2-3 mm in thickness). These disks were heat-sealed in 25-micron-thick fluorinated ethyle-nepropylene resin film smaller than 14 mm X 14 mm. A Compton suppression prompt gamma activation spectrum was accumulated for 2000-9000 s. JB-1 and JB-2 were used to calibrated the element contents. Details of the analytical procedures have been described by Sano et al. (1999, 2006). Replicate analysis of JB-1 and JB-2 indicate overall precision and accuracy on the order of 3% for B, Ti and Gd, 5% for K, and 10% for Sm (Sano et al., 1999, 2006). Accuracy of the PGNA was also checked by comparison of TiO$_2$ and K$_2$O values with XRF analyses (Table 2). The comparison shows that there is a good agreement between the PGNA and XRF within 0.06 wt % for TiO$_2$ and 0.27 wt % for K$_2$O. Although the difference is a little bit higher than analytical precision and accuracy (0.04 wt % for TiO$_2$ and 0.22 for K$_2$O; Sano et al., 2006), it does not significantly affect the conclusion of this study.

Results

True density, apparent density, porosity, mode of phenocryst, and whole rock compositions of Hoei rocks are listed in Table 2. Average compositions of the hornblende phenocryst are SiO$_2$, 48.43; TiO$_2$, 1.28; Al$_2$O$_3$, 6.06; FeO, 13.74; MnO, 0.61; MgO, 14.50; CaO, 10.63; Na$_2$O, 1.49; K$_2$O, 0.36 in weight percent. The mineral compositions are used for calculation of fractional crystallization (see Discussion). Here we report detailed petrography, variation of density and porosity, and whole rock compositions.

Petrography

Unit I (subunits A–C): Pumice rocks from Unit I are highly vesicular (porosity >70 vol.%) and aphyric to sparsely plagioclase-orthopyroxene phyric dacite clasts. Two thin sections contain hornblende phenocrysts (Table 1; Fig. 3B). There is no special note for difference of petrography among the three subunits (A to C) in Unit I. Although phenocryst mode is small (<1 vol.%), plagioclase is the most abundant phenocryst phase, usually present as euhedral to subhedral with tabular shape. A few plagioclase phenocrysts contain

Table 2.   whole rock compositions of Hoei pumice, scoria and lithic fragments from Fuji Volcano.

Sample	FJ19-A1	FJ19-A3	FJ19-A4	FJ19-A5	FJ19-A6	FJ19-A7	FJ19-A8	FJ19-B1	FJ19-B2	FJ19-B4	FJ19-B5	FJ19-B7	FJ19-C1
Unit[a]	Ia	Ia	Ia	Ia	Ia	Ia	Ia	Ia	Ia	Ia	Ia	Ia	Ib
Height (cm)[b]	10	10	10	10	10	10	10	25	25	25	25	25	39
True ρ (g/cm^3)							2.49(4)						
Apparent ρ (g/cm^3)	0.80(5)	0.35(2)	0.53(4)	0.54(2)	0.58(1)	0.55(2)	0.62(1)	0.67(7)	0.79(13)	0.56(1)	0.36(2)	0.32(1)	0.56(2)
Porosity (%)							75(2)						
Phenocryst[c]	a	op	op	op	pl	pl,op	pl,op	a	pl,op	a	pl	a	pl,hb
Mode (%)[d]	0	<<1	<<1	<<1	<<1	<<1	<<1	0	<<1	0	<<1		<<1
XRF laboratory[e]	NM	FU	FU	FU	FU	FU	FU	FU	FU	NM	FU	FU	FU
wt %													
SiO$_2$	64.92	66.84	63.84	65.20	63.49	64.11	65.06	65.50	61.68	65.75	63.60	62.43	60.03
TiO$_2$	0.78	0.67	0.83	0.76	0.86	0.82	0.79	0.76	0.96	0.71	0.83	0.91	1.00
Al$_2$O$_3$	15.57	15.30	15.87	15.61	15.94	15.81	15.69	15.62	16.25	15.33	15.88	16.16	16.36
Fe$_2$O$_3$[f]	5.81	4.99	6.43	5.74	6.62	6.28	6.00	5.73	7.35	5.26	6.31	6.96	7.80
MnO	0.11	0.10	0.13	0.11	0.13	0.12	0.12	0.11	0.15	0.10	0.13	0.14	0.15
MgO	1.79	1.40	1.95	1.67	1.96	1.88	1.82	1.69	2.27	1.55	1.89	2.08	2.42
CaO	4.57	3.87	4.81	4.37	4.89	4.72	4.55	4.40	5.47	4.21	4.75	5.06	5.65
Na$_2$O	3.91	3.78	3.81	3.83	3.84	3.88	3.86	3.85	3.87	3.87	3.82	3.82	3.76
K$_2$O	2.33	2.58	2.17	2.35	2.12	2.19	2.30	2.36	1.88	2.56	2.16	1.99	1.74
P$_2$O$_5$	0.22	0.18	0.23	0.21	0.24	0.23	0.22	0.21	0.28	0.20	0.23	0.26	0.29
LOI	0.50									1.03			
Total	100.51	99.71	100.07	99.85	100.09	100.04	100.41	100.23	100.16	100.57	99.60	99.81	99.20
ppm													
Rb	56.7	61	49	54	47	50	52	53	43		48	43	39
Ba	437	505	435	467	434	479	502	477	498		424	450	430
Nb	2.0	3	3	4	3	4	4	3	4		3	4	4
Pb	9	10	9	7	9	7	9	10	9		9	5	6
Sr	330	279	321	304	329	320	308	306	341		320	334	331
Zr	182	192	172	184	175	177	179	183	155		177	171	141
Y	38	35	33	33	34	32	32	34	33		33	33	31
Ce	44												
Cr	7	4	3	3	4	4	3	3	6		2	5	3
Ni	2	7	6	8	5	9	8	7	14		6	9	18
Co	16												
V	130	89	124	115	125	126	114	109	154		130	138	167
Th	4.6												
Zn	90												
S	9												
PGNA													
TiO$_2$ (wt %)	0.83(3)[g]			0.74(1)	0.83(2)	0.81(2)	0.75(2)	0.75(3)	0.91(2)				0.95(1)
K$_2$O (wt %)	2.06(5)			2.37(9)	2.15(8)	2.23(8)	2.38(6)	2.36(5)	1.93(4)				1.76(4)
B (ppm)	28.2(6)			26.2(8)	26.3(7)	27.4(7)	26.2(6)	27.0(5)	28.6(6)				30.2(6)
Cl (ppm)	795(66)			634(63)	593(58)	600(58)	795(66)	704(58)	689(57)				811(66)
Gd (ppm)	6.08(13)			5.78(20)	5.86(19)	5.91(18)	5.89(15)	6.09(11)	6.18(12)				6.06(11)
Sm (ppm)	5.62(20)			5.85(29)	5.82(27)	5.73(26)	5.67(19)	5.59(18)	5.69(19)				5.66(18)
INAA (ppm)													
La	16.09(29)						15.98(29)	15.60(28)		15.84(23)			16.16(29)
Ce	37.6(9)						39.9(9)	39.9(9)		36.1(5)			35.2(9)
Nd	27(9)						24(8)	27(8)		25(4)			27(8)
Sm	6.16(23)						6.11(23)	5.93(23)		5.75(4)			6.52(23)
Eu	1.47(2)						1.42(2)	1.37(2)		1.23(3)			1.63(3)
Yb	3.63(37)						3.48(33)	3.63(37)		3.35(6)			3.65(35)
Lu	0.28(6)						0.40(7)	0.47(8)		0.55(1)			0.39(7)
Cs	2.26(11)						2.58(11)	2.38(11)		2.36(7)			2.04(12)
Th	3.69(5)						4.27(5)	4.21(5)		4.06(5)			3.03(5)
Hf	4.85(7)						5.10(6)	4.94(6)		4.66(7)			4.42(6)
Cr	5.5(5)						4.0(5)	4.1(4)		28.9(9)			5.6(5)

[a] Unit boundaries are based on Miyaji (1984). [b] Middle height of each subunit from the base of the Hoei pumice and scoria. [c] Abbreviations of phases are ol, olivine; pl, plagioclase; cp, clinopyroxene (augite), op, orthopyroxene (hypersthene), hb, hornblende; mt, magnetite and ilmenite. Abbreviation of "a" shows aphyric with no phenocryst. Microphenocryst is also included. [d] Mode of phenocrysts are determined based on a method of Terry and Chilingar (1955). [e] XRF analyses were conducted on two laboratories: NM, National museum of Nature and Science; FU, Fuji Tokoha University. [f] Total iron expressed as Fe$_2$O$_3$. [g] Numbers in parentheses adjacent are 1 standard deviation; e.g. 0.83(3) represents 0.83 ± 0.03 wt %. Standard deviations are due to counting statistics only. [h] An average value of 17 measurements (n=17) of standard JB-1a (a standard rock from the Geological Survey of Japan) for XRF analysis. For PGNA, the value is from Sano et al. (1999, 2006). [i] Recommended value of the JB-1a (Imai et al., 1995). [j] One standard deviation of a calibration line for each element.

Table 2 (continued)

Sample	FJ19-C4	FJ19-C5	FJ19-D1	FJ19-D3	FJ19-E1	FJ19-F1	FJ19-F1	FJ19-F2	FJ19-F5	FJ19-G1	FJ19-G2	FJ19-G3	FJ19-G4
Unit	Ib	Ib	II	II	II	II		II	II	II	II	II	II
Height (cm)	39	39	65	65	73	89		89	89	106	106	106	106
True ρ (g/cm³)			2.73(9)	2.39(12)	2.46(15)	2.81(6)		2.67(11)		2.68(7)			
Apparent ρ (g/cm³)	0.48(1)	0.32(3)	1.89(8)	0.82(7)	1.14(5)	2.35(11)		2.17(3)	2.18(16)	1.41(6)	1.97(10)	1.67(5)	1.69(10)
Porosity (%)			31(2)	66(7)	54(4)	16(1)		19(1)		47(2)			
Phenocryst	a	hb	pl,op	a	pl,ol,op,mt	ol,pl,cp,op		ol,pl,cp,op	ol,pl,cp,op	ol,pl,mt	pl	ol,pl	pl
Mode (%)	0	<<1	<<1	<<1	2	15		7	10	2	1	1	1
XRF laboratory	NM	NM	FU	FU	FU	NM	FU	FU	NM	FU	NM	NM	NM
wt %													
SiO₂	66.26	62.71	56.77	66.37	57.88	50.49	50.81	50.33	50.05	56.41	56.62	56.50	56.57
TiO₂	0.72	0.85	1.24	0.70	1.16	0.95	0.94	1.27	0.98	1.22	1.23	1.21	1.20
Al₂O₃	15.38	15.93	16.75	15.37	16.65	18.15	18.04	17.24	17.43	16.76	16.91	16.99	16.93
Fe₂O₃	5.18	6.46	9.94	5.27	9.22	10.61	10.86	12.06	10.9	9.92	9.60	9.56	9.73
MnO	0.10	0.13	0.18	0.11	0.17	0.16	0.16	0.18	0.17	0.18	0.17	0.17	0.17
MgO	1.48	2.03	3.40	1.58	3.18	6.36	6.32	5.94	6.75	3.43	3.33	3.46	3.43
CaO	4.16	4.96	7.05	4.13	6.68	10.31	10.29	10.40	10.88	7.09	7.10	7.15	7.12
Na₂O	3.77	3.80	3.70	3.82	3.68	2.92	2.71	2.57	2.45	3.61	3.64	3.67	3.78
K₂O	2.61	2.14	1.32	2.50	1.44	0.46	0.44	0.55	0.4	1.31	1.34	1.31	1.32
P₂O₅	0.21	0.25	0.35	0.19	0.33	0.13	0.14	0.21	0.14	0.34	0.35	0.34	0.35
LOI	0.29	0.58				-0.20			-0.03		-0.31	-0.31	-0.24
Total	100.16	99.84	100.70	100.04	100.39	100.34	100.71	100.75	100.12	100.27	99.98	100.05	100.36
ppm													
Rb	61.5		25	57	30	6.7	8	9		26	28.4		
Ba	456		374	495	386	149	172	183		351	326		
Nb	2.0		4	4	4	1.7	1	3		3	2.1		
Pb	10		8	8	5	3.3	0	2		7	7		
Sr	314		393	259	383	386	393	333		393	390		
Zr	187		143	160	147	78	61	75		140	144		
Y	39		32	32	30	17	17	21		30	33		
Ce	45					16					33		
Cr	4		14	3	10	100	100	86		15	13		
Ni	6		5	16	7	36	36	30		7	ld		
Co	14					37					30		
V	116		207	112	194	280	300	346		211	234		
Th	5.7					0.9					2.3		
Zn	82					74					127		
S	13					ld					1		
PGNA													
TiO₂ (wt %)			1.19(2)	0.67(2)	1.14(1)	0.92(1)		1.26(2)		1.18(2)			
K₂O (wt %)			1.32(3)	2.56(5)	1.46(3)	0.49(3)		0.56(2)		1.30(3)			
B (ppm)			29.5(6)	33.4(6)	29.5(6)	9.9(3)		16.3(3)		27.2(7)			
Cl (ppm)			764(62)	774(63)	682(56)	173(20)		247(21)		387(53)			
Gd (ppm)			6.24(11)	6.00(11)	6.26(12)	2.55(9)		4.11(8)		5.86(9)			
Sm (ppm)			5.57(17)	5.65(18)	5.69(18)	2.26(11)		3.47(13)		5.55(16)			
INAA (ppm)													
La	14.76(20)	13.45(20)	12.61(25)	15.99(28)	14.86(27)	4.30(16)			4.23(15)		13.87(18)	13.46(97)	13.20(18)
Ce	35.6(4)	29.6(4)	33.5(9)	40.4(9)	37.6(1.0)	10.7(8)			11.3(4)		36.7(5)	34.3(5)	30.5(4)
Nd	27(4)	25(4)	25(9)	25(8)	30(10)	11(7)			11(4)		22(3)	22(4)	21(3)
Sm	5.28(4)	5.29(4)	5.78(22)	6.22(23)	6.55(24)	2.37(13)			2.62(4)		5.84(4)	5.42(27)	5.85(4)
Eu	1.20(3)	1.19(3)	1.67(3)	1.33(2)	1.82(3)	0.83(2)			0.94(3)		1.83(5)	1.77(4)	1.61(4)
Yb	3.13(5)	2.83(5)	3.08(32)	4.10(37)	3.69(40)	1.07(12)			1.68(6)		3.14(6)	2.98(7)	3.00(5)
Lu	0.53(1)	0.48(1)	0.39(6)	0.55(8)	0.50(9)	0.21(6)			0.26(7)		0.49(1)	0.48(1)	0.50(1)
Cs	2.31(6)	1.89(7)	1.54(12)	2.70(11)	1.86(13)	0.44(12)			0.45(7)		1.49(7)	1.54(8)	1.39(7)
Th	4.04(5)	2.87(4)	2.03(5)	4.85(5)	2.70(6)	0.51(6)			0.58(6)		2.29(6)	2.17(5)	2.08(5)
Hf	4.69(7)	3.86(6)	3.63(6)	5.57(7)	4.39(7)	1.27(6)			1.46(7)		3.89(7)	3.75(8)	3.51(7)
Cr	22.0(1.0)	27.5(9)	11.4(6)	8.6(4)	13.9(6)	86.8(8)			149(2)		25.0(1.1)	37.7(1.6)	27.9(1.1)

Table 2 (continued)

Sample	FJ19-H1	FJ19-H1	FJ19-H3	FJ19-H3	FJ19-H5	FJ19-I1	FJ19-I2	FJ19-I3	FJ19-I4	FJ19-I5	FJ19-J1	FJ19-J1	FJ19-J2
Unit	II	II	II		II	III	III	III	III	III	III		III
Height (cm)	117	117	117		117	133	133	133	133	133	149		149
True ρ (g/cm^3)	2.63(4)		2.78(3)			2.79(12)	2.80(5)				2.80(13)		2.70(9)
Apparent ρ (g/cm^3)	1.52(4)		2.17(7)		1.96(5)	1.43(5)	1.54(12)	1.43(1)	1.93(7)	1.04(9)	2.08(12)		1.41(9)
Porosity (%)	42(1)		22(1)			49(3)	45(4)				26(2)		48(3)
Phenocryst	ol,pl,op		ol,pl,op		ol,pl,op	ol,pl	ol,pl,op	ol,pl	pl,op	pl,op	ol,pl,cp,mt	a	ol,pl
Mode (%)	10		15		10		20	3	15	1		0	1
XRF laboratory	NM	FU	NM	FU	NM	FU	FU	NM	NM	NM	NM	FU	FU
wt %													
SiO$_2$	56.33	56.36	56.18	56.18	50.78	51.71	50.93	51.32	50.67	51.19	51.93	52.16	50.16
TiO$_2$	1.22	1.24	1.27	1.29	1.09	1.34	1.25	1.35	1.27	1.34	1.35	1.36	1.32
Al$_2$O$_3$	16.90	16.78	16.93	16.84	17.44	16.69	16.57	16.98	17.07	17.02	16.87	16.75	16.96
Fe$_2$O$_3$	9.81	10.05	9.75	10.00	11.38	11.96	11.59	11.79	11.97	11.78	11.92	12.12	12.08
MnO	0.18	0.18	0.18	0.18	0.18	0.18	0.18	0.18	0.18	0.18	0.18	0.19	0.18
MgO	3.45	3.44	3.56	3.54	5.65	5.07	6.24	5.18	6.07	5.19	4.85	4.86	6.52
CaO	7.12	7.10	7.16	7.14	10.14	9.50	9.87	9.61	9.81	9.57	9.20	9.17	10.07
Na$_2$O	3.63	3.67	3.65	3.68	2.70	2.81	2.70	2.86	2.74	2.75	2.97	2.93	2.56
K$_2$O	1.30	1.30	1.29	1.27	0.57	0.81	0.68	0.78	0.65	0.78	0.86	0.86	0.56
P$_2$O$_5$	0.35	0.35	0.35	0.35	0.19	0.25	0.23	0.25	0.22	0.25	0.26	0.26	0.21
LOI	-0.21		-0.05		-0.31			-0.42	-0.49	-0.21	-0.47		
Total	100.08	100.47	100.27	100.47	99.81	100.32	100.24	99.88	100.16	99.84	99.92	100.66	100.62
ppm													
Rb	27.9	26	27.0	24	9.8	15	15	14.3			16.3	15	10
Ba	326	359	317	330	166	212	213	200			211	216	220
Nb	2.1	4	2.2	4	1.7	2	3	1.7			1.7	3	2
Pb	7	6	7	6	4	5	0	5			6	6	1
Sr	393	392	391	393	324	355	383	342			345	359	342
Zr	142	140	141	139	79	90	80	93			98	92	78
Y	33	31	33	30	21	23	18	24			25	23	21
Ce	34		36		18			24			25		
Cr	14	13	14	13	72	48	114	43			32	33	128
Ni	1	7	2	7	16	13	39	10			5	10	51
Co	31		32		42			42			40		
V	238	207	250	215	345	376	335	396			381	360	373
Th	1.6		2.5		0.3			0.9			1.1		
Zn	129		130		94			105			105		
S	11		8		1			8			3		
PGNA													
TiO$_2$ (wt %)	1.19(2)		1.22(2)			1.33(2)	1.21(2)				1.32(2)		1.28(2)
K$_2$O (wt %)	1.30(5)		1.21(4)			0.80(2)	0.67(2)				0.87(2)		0.53(3)
B (ppm)	29.4(7)		27.9(7)			17.4(3)	16.2(3)				18.0(3)		17.2(4)
Cl (ppm)	626(58)		608(58)			454(38)	184(17)				407(34)		368(37)
Gd (ppm)	5.89(18)		5.84(15)			4.37(8)	3.75(7)				4.50(8)		3.82(10)
Sm (ppm)	5.44(20)		5.59(19)			3.96(9)	3.43(8)				4.18(9)		3.38(13)
INAA (ppm)													
La	14.62(27)		13.46(25)		5.12(13)	8.96(20)		6.84(13)	5.59(11)	7.57(12)			7.63(18)
Ce	31(1.0)		29.6(9)		12.8(5)	22.9(9)		14.5(4)	15.1(4)	17.3(5)			18.3(9)
Nd	25(9)		30(9)		11(3)	20(8)		ld	ld	17(4)			12(7)
Sm	6.48(24)		5.89(22)		2.90(3)	4.44(18)		3.32(3)	2.95(3)	3.78(3)			3.96(17)
Eu	1.75(3)		1.70(3)		0.94(3)	1.42(3)		1.03(3)	0.98(3)	1.19(4)			1.35(3)
Yb	3.61(41)		3.65(38)		1.68(5)	2.64(33)		1.89(5)	1.66(4)	2.02(4)			2.52(36)
Lu	0.44(7)		ld		0.25(1)	ld		0.30(1)	0.26(1)	0.33(1)			0.21(15)
Cs	1.68(14)		1.50(13)		0.50(8)	0.97(17)		0.80(7)	0.58(7)	0.62(7)			0.74(14)
Th	2.21(5)		2.06(5)		0.80(5)	1.24(6)		1.12(6)	0.67(5)	1.00(6)			0.80(6)
Hf	3.78(6)		3.76(6)		1.50(6)	2.58(7)		1.79(6)	1.62(6)	1.97(6)			2.07(6)
Cr	11.9(6)		12.6(5)		71.9(1.7)	41.0(7)		46.1(1.2)	74.9(1.5)	42.8(1.3)			131.7(9)

Table 2 (continued)

Sample	FJ19-J3	FJ19-K1	FJ19-L1	FJ19-L1	FJ19-L2	FJ19-L3	FJ19-M1	FJ19-N1	FJ19-O1	FJ19-O1	FJ19-P2	FJ19-Q1	FJ19-Q2
Unit	III	III	III		III	III	IV	IV	IV		IV	IV	IV
Height (cm)	149	166	182		182	182	205	235	255		273	288	288
True ρ (g/cm^3)		2.81(7)	2.89(6)				2.87(6)		2.93(9)			2.62(44)	
Apparent ρ (g/cm^3)	2.26(8)	1.28(10)	1.74(7)		2.01(9)	1.84(7)	0.97(3)		0.89(4)			0.67(4)	0.97(5)
Porosity (%)		54(4)	40(2)				66(2)		70(4)			74(13)	
Phenocryst	ol,pl,cp,op	ol	ol,pl,mt		ol,pl,cp	pl	pl,mt	pl	pl,ol		ol,pl	ol,pl	a
Mode (%)	3	<<1	15		2	<<1	<<1	<<1	2		1	2	0
XRF laboratory	NM	FU	NM	FU	NM	NM	FU	FU	NM	FU		FU	FU
wt %													
SiO$_2$	51.81	51.61	50.63	50.86	51.50	51.09	51.58	51.33	51.08	51.31		51.20	51.18
TiO$_2$	1.31	1.34	1.51	1.52	1.34	1.34	1.35	1.35	1.34	1.35		1.35	1.35
Al$_2$O$_3$	16.84	16.80	16.54	16.43	17.02	16.88	16.82	16.94	16.99	16.83		16.81	16.90
Fe$_2$O$_3$	11.63	12.05	12.71	12.85	11.83	11.75	11.99	11.94	11.95	12.09		11.98	12.15
MnO	0.18	0.19	0.19	0.19	0.18	0.18	0.19	0.19	0.18	0.19		0.19	0.18
MgO	4.99	5.14	5.82	5.73	5.24	5.20	5.16	5.25	5.27	5.29		5.26	5.21
CaO	9.36	9.62	9.73	9.68	9.68	9.62	9.60	9.60	9.73	9.69		9.68	9.72
Na$_2$O	2.91	2.80	2.37	2.32	2.85	2.79	2.76	2.71	2.74	2.74		2.71	2.72
K$_2$O	0.86	0.78	0.57	0.57	0.78	0.78	0.77	0.75	0.79	0.75		0.74	0.75
P$_2$O$_5$	0.25	0.25	0.31	0.31	0.25	0.25	0.25	0.25	0.25	0.24		0.24	0.24
LOI	-0.44		-0.52		-0.45	-0.14			-0.59				
Total	99.7	100.58	99.86	100.46	100.22	99.74	100.47	100.31	99.73	100.48		100.16	100.40
ppm													
Rb	15.8	15	15.1	15	14.4	14.4	14	14	13.9	14		14	14
Ba	204	241	228	259	190	195	239	246	189	193		205	199
Nb	1.8	2	1.7	3	1.9	1.8	3	2	2.1	2		2	3
Pb	5	3	6	5	5	5	5	3	5	5		3	4
Sr	340	359	294	311	338	340	357	360	339	358		360	360
Zr	96	88	98	102	93	94	87	87	92	87		86	86
Y	25	23	27	26	24	24	23	22	23	23		22	23
Ce	26		27		21	23			26				
Cr	40	48	74	80	47	46	49	46	49	51		48	46
Ni	7	12	22	27	8	7	13	17	7	14		15	14
Co	41		43		41	42			41				
V	381	373	391	377	398	396	378	373	399	374		387	376
Th	1.0		1.4		1.8	2.1			1.1				
Zn	102		102		103	104			106				
S	ld		ld		1	1			1				
PGNA													
TiO$_2$ (wt %)		1.31(2)	1.47(3)				1.29(3)		1.31(3)			1.32(3)	
K$_2$O (wt %)		0.80(2)	0.59(2)				0.78(2)		0.76(2)			0.73(2)	
B (ppm)		17.5(3)	21.8(4)				17.0(3)		17.5(3)			17.5(3)	
Cl (ppm)		479(40)	305(26)				439(37)		465(39)			498(42)	
Gd (ppm)		4.25(8)	5.09(9)				4.24(7)		4.28(8)			4.25(7)	
Sm (ppm)		3.83(9)	4.46(10)				3.83(9)		3.87(9)			3.77(9)	
INAA (ppm)													
La							7.98(18)		9.23(20)		7.04(12)	8.48(18)	
Ce							18.7(9)		21.6(9)		16.9(4)	18.6(8)	
Nd							16(7)		21(8)		18(4)	16(7)	
Sm							3.87(16)		4.64(19)		3.59(3)	4.15(17)	
Eu							1.26(2)		1.44(3)		1.16(3)	1.25(2)	
Yb							1.89(35)		2.90(39)		1.96(5)	2.55(38)	
Lu							ld		ld		0.31(1)	ld	
Cs							0.90(14)		0.99(15)		0.65(6)	0.90(14)	
Th							1.07(5)		1.30(6)		0.95(5)	1.03(5)	
Hf							2.24(6)		2.56(7)		1.91(6)	2.23(6)	
Cr							36.0(7)		49.2(8)		49.5(1.6)	37.0(6)	

Table 2   (continued)

Sample	FJ19-Q3	FJ19-Q4	FJ19-Q5	FJ19-Q8	FJ19-R1	FJ19-R1	FJ19-R3	FJ55	JB-1a[h] (n=17)	JB-1a[i] recom.	1sigma[j]
Unit	IV	IV	IV	IV	IV		IV				
Height (cm)	288	288	288	288	318		318				
True ρ (g/cm^3)					2.82(10)			2.89(4)			
Apparent ρ (g/cm^3)	0.55(3)	1.16(14)	0.84(5)	0.97(12)	0.94(7)		1.70(9)	2.07(18)			
Porosity (%)					67(5)			28(3)			
Phenocryst	pl	pl	ol,pl	ol,pl	ol,pl		ol,pl	ol,pl			
Mode (%)	<<1	<<1	<<1	2	1		2	5			
XRF laboratory	FU	FU	FU	FU	NM	FU	NM	NM	NM		
wt %											
SiO$_2$	51.19	51.27	51.09	51.14	50.81	50.86	50.98	50.81	52.41	52.41	0.299
TiO$_2$	1.36	1.36	1.36	1.35	1.35	1.35	1.36	1.39	1.31	1.28	0.023
Al$_2$O$_3$	16.96	16.96	16.92	16.87	17.09	16.89	17.02	16.84	14.48	14.45	0.136
Fe$_2$O$_3$	12.06	12.03	12.05	12.00	11.87	12.07	11.96	12.14	9.01	9.05	0.140
MnO	0.19	0.19	0.19	0.19	0.18	0.18	0.18	0.18	0.14	0.148	0.004
MgO	5.22	5.26	5.31	5.33	5.28	5.33	5.29	5.32	7.80	7.83	0.165
CaO	9.70	9.69	9.70	9.75	9.64	9.61	9.76	9.75	9.37	9.31	0.059
Na2O	2.68	2.67	2.63	2.67	2.72	2.61	2.76	2.86	2.75	2.73	0.092
K$_2$O	0.74	0.74	0.74	0.74	0.75	0.72	0.77	0.76	1.43	1.40	0.050
P$_2$O$_5$	0.24	0.24	0.24	0.24	0.26	0.25	0.26	0.26	0.26	0.26	0.007
LOI					-0.10		-0.33	-0.35	0.64	0.92	
Total	100.34	100.41	100.23	100.28	99.85	99.87	100.01	99.96	99.60		
ppm											
Rb	15	15	14	14	13.1	14		13.7	40.0	39.2	2.4
Ba	197	230	231	193	196	206		189	494	504	19
Nb	2	2	2	3	1.7	3		1.8	24.2	26.9	2.1
Pb	4	5	4	3	5	4		5	6.0	6.76	1.3
Sr	359	355	358	355	338	355		345	436	442	19.0
Zr	86	84	85	84	92	86		93	146	144	8.6
Y	22	22	22	22	24	23		24	22	24	2.0
Ce					23			20	58	65.9	4.1
Cr	45	46	48	61	47	47		44	374	392	17
Ni	16	13	15	15	10	16		9	136	139	7.1
Co					43			43	33	38.6	3.4
V	380	377	377	371	410	379		400	217	205	5.8
Th					1.7			0.6	8.8	9.03	0.5
Zn					106			102	77	82.1	5.1
S					6			ld	12	10.2	6.5
PGNA											
TiO$_2$ (wt %)					1.35(3)			1.33(2)	1.27	1.28	
K$_2$O (wt %)					0.76(2)			0.72(3)	1.39	1.40	
B (ppm)					17.8(3)			17.7(4)	7.75	7.88	
Cl (ppm)					528(43)			241(26)			
Gd (ppm)					4.58(7)			4.23(10)	4.64	4.67	
Sm (ppm)					3.84(11)			3.85(13)	5.17	5.07	
INAA (ppm)											
La					10.01(21)		8.12(12)	7.34(17)			
Ce					22.9(1.0)		30.5(5)	16.2(8)			
Nd					20(8)		21(4)	14(6)			
Sm					4.96(20)		4.03(3)	3.69(16)			
Eu					1.59(3)		1.27(3)	1.10(2)			
Yb					2.67(41)		2.15(4)	1.80(29)			
Lu					0.18(14)		0.35(1)	0.29(19)			
Cs					1.14(17)		0.77(6)	0.74(74)			
Th					1.15(7)		0.99(5)	0.86(5)			
Hf					2.61(7)		2.22(6)	1.84(6)			
Cr					51.4(8)		49.9(1.4)	32.3(7)			

apatite with needle shape, as firstly reported by Watanabe *et al*. (2006). Orthopyroxene is the next abundant phenocrysts with euhedral and tabular shape (Fig. 3A). One hornblende phenocryst is large (Fig. 3B; 300 micron wide and 800 micron length), but others are as small as microphenocryst size (<100 micron wide). The largest hornblende contains inclusions of ilmenite and zircon (Fig. 4). Groundmass is mainly composed of glass partly devitrified to mesostasis. Acicular plagioclase and tiny skeletal magnetite also present in groundmass.

Unit II (subunits D–H): In contrast to Unit I, volcanic rocks from Unit II are various: pumice clasts, scoria clasts, and lithic fragments. Main constitute rocks in subunit layers differ from one to another, and therefore, we report petrography of the each subunit layer below.

Subunits D and E layers consist of moderately vesicular (porosity ~30 vol.%) scoria and highly vesicular (porosity ~70 vol.%) pumice. The scoria is aphyric, sparsely plagioclase-orthopyroxene phyric, and sparsely plagioclase-orthopyroxene-olivine phyric (up to 2 vol.%) andesite. Plagioclase phenocrysts are tabular and rarely form glomerocrysts. Orthopyroxene phenocrysts are euhedral to subhedral. Olivine phenocrysts are rare in the thin sections (several grains per thin section) and subhedral to anhedral shape with overgrowth of orthopyroxene in their rims. Magnetite, rhomb to skeletal shape, is observed as microphenocrysts. Groundmasses in the andesite scoria have trachytic texture consisting of acicular plagioclase, tiny skeletal magnetite, and mesostasis. Petrography of dacite pumice in subunits D and E is nearly identical to that of Unit I.

Most volcanic rocks from subunit F layer are lithic fragments. All 5 rocks in this subunit (FJ19-F1 to F5) are of low to sparsely vesicular (porosity <20 vol. %) lithic fragments. They are moderately to highly plagioclase-olivine-orthopyroxene-clinopyroxene phyric (7–15 vol.%) basalts. Plagioclase phenocrysts are equant to platy or irregularly shaped. Most large crystals (>1 mm wide) are equant to subequant and have dusty interiors showing sieved texture. They consist of devitrified melt inclusions, fibrous pyroxenes, and tiny magnetites. On the other hand, smaller tabular plagioclase phenocrysts have clear cores. Some irregular-shaped plagioclase phenocrysts form glomerocrysts, and a few of them exhibit complex sequences of skeletal growth and oscillatory zoning. Olivine phenocrysts are euhedral and skeletal shape and commonly contain spinel and rare melt inclusions. In many cases, iddingsite replaces the olivine phenocrysts along cracks and rims. Orthopyroxene phenocrysts are euhedral and elongate shape. Clinopyroxene is present as only microphenocrysts (<300 micron) with subhedral to anhedral crystals. In groundmasses of the lithic fragments, holocrystalline intersertal textures predominate, where branching acicular plagioclases are intergrown with smaller fibrous pyroxenes, rhomb to skeletal magnetite, and acicular ilmenite. Grain sizes of all these lithic fragments are distinctly larger and crystallinities are apparently higher than those of essential scoria clasts, indicating that the 5 subunit F rocks are accessory fragments.

Unit G layer is mainly composed of moderately vesicular (porosity ~40 vol.%) scoria. These are sparsely plagioclase-phyric and plagioclase-olivine phyric (1–2 vol.%) basalts. Most plagioclase phenocrysts are subhedral and equant to subequant shape. A few dusty plagioclase phenocrysts having devitrified melt inclusions are also present. Olivine phenocrysts are subhedral and rounded shape, implying resorption. On the other hand, magnetite occurs only as microphenocrysts (<100 micron) and its typically tiny skeletal shape. Groundmasses are cryptocrystalline and are composed of acicular and bladed plagioclase, tiny anhedral pyroxenes, skeletal magnetite, glass, and mesostasis.

Andesite scoria clasts from Subunit H layer are characterized by their relatively high content of phenocrysts (10–15 vol.%). They are moderately vesicular (porosity ~40 vol. %) and moderately plagioclase-olivine-orthopyroxene phyric andesite. Plagioclase phenocrysts are tabular, subequant, or irregular shaped and sometimes form
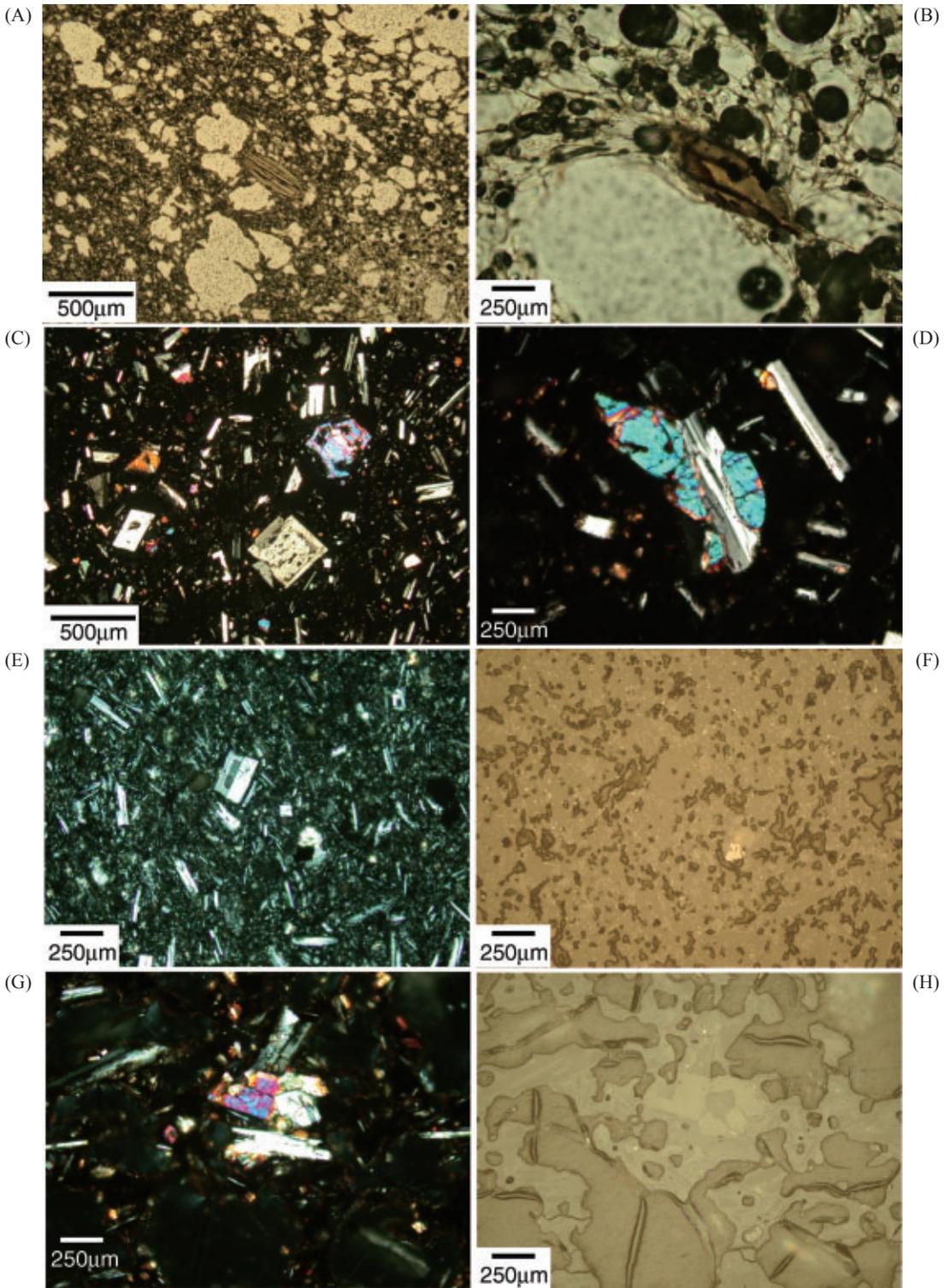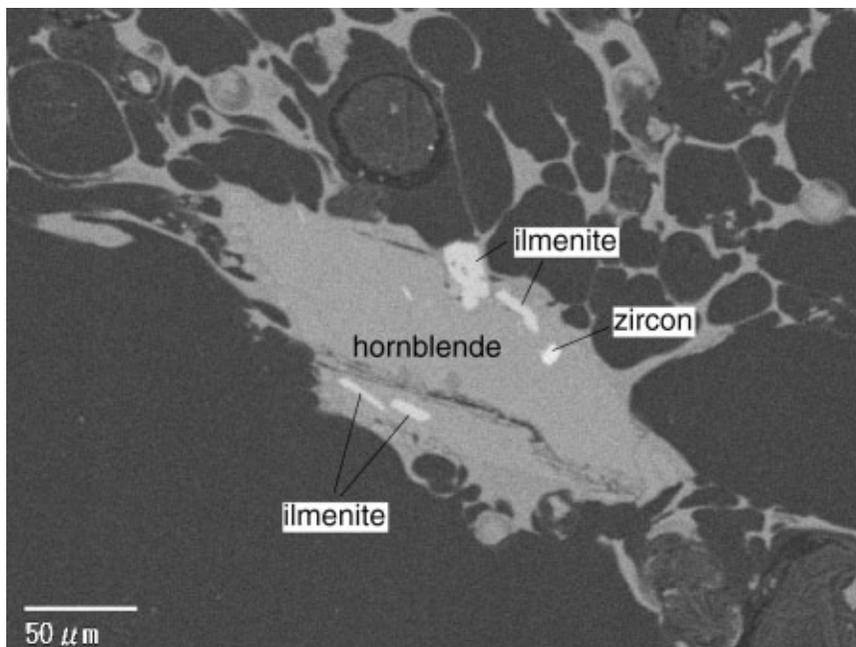
Fig. 4.   Backscattered electron microprobe image of a hornblende phenocryst in a dacite clast (FJ19-C5). The phenocryst includes ilmenite and zircon inclusions.

Fig. 3.   Photomicrographs of thin sections from volcanic rocks, Hoei eruption. A, orthopyroxene (hypersthene) phenocryst in FJ19-A4 dacite, plane-polarized light; B, hornblende phenocryst in FJ19-C5 dacite from Unit I, plane-polarized light; C, typical petrography of moderately plagioclase-olivine-orthopyroxene phyric andesite (FJ19-H5) from Unit II. Skeletal olivine phenocrysts (middle right), tabular plagioclase phenocryst with devitrified inclusions (lower center), orthopyroxene phenocryst (orange crystal in middle left) wrapping around acicular plagioclase can be seen, crossed-polarized light; D, typical olivine-plagioclase intergrowth set in FJ19-H5 andesite from Unit II, crossed-polarized light; E, typical petrography of moderately olivine-plagioclase-orthopyroxene basalt (FJ-19-J3) from Unit III. An equant plagioclase phenocryst shows reverse zoning (center), crossed-polarized light; F, same view as E, but in reflected light to show a skeletal magnetite microphenocryst (a white mineral in size of ~100 micron) and hundreds of tiny magnetite minerals (white dots); G, Typical petrography of sparsely olivine-plagioclase basalt (FJ19-R1) from Unit IV. Olivine phenocrysts are intergrown with partly skeletal, subhedral plagioclase phenocrysts (center), crossed-polarized light; H, same view as E, but in reflected light to show only a few magnetite minerals (white) are present in a field of view. Volatile (non-reflective, dark gray) content in Unit IV is distinctly higher than that in Unit III (in F).

multi-crystalline aggregates and glomerocrysts. Some have skeletal interior or occur as broken zoned fragments, or occur as dusty crystals (including needle apatite) with devitrified inclusions (Fig. 3C). Olivine phenocrysts are euhedral to subhedral and several crystals shows skeletal shape (Fig. 3C). Some olivine phenocrysts are intergrown with tabular or elongate plagioclase (Fig. 3D). Orthopyroxene phenocrysts are subequant to tabular shape and commonly wrapping around acicular plagioclase (Fig. 3C). Groundmasses of subunit H scoria are nearly identical to those of subunit G.

Unit III (subunits I–L): As described above, petrographical characteristics of Unit II are similar within the same subunit layers. On the other hand, those of Unit III vary from one rock to the next within individual subunit layers. Although phenocryst assemblage and mode of Unit III rocks are various, all the rocks are moderately vesicular (porosity is 30–50 %) basalt scoria and have nearly identical groundmass appearances. Thus, we report the petrography of Unit III rocks simultaneously.

The Unit III scoria clasts are sparsely olivine phyric (<1 vol.%), sparsely plagioclase phyric (<1 vol.%), sparsely to highly olivine-plagioclase phyric (1–15 vol.%), sparsely to highly plagioclase-orthopyroxene phyric (1–15 vol.%), and moderately to highly olivine-plagioclase-orthopyroxene phyric (3–20 vol.%) basalts. Generally, mode of phenocryst increases with increasing number of phenocryst phase. Plagioclase, olivine and orthopyroxene phenocrysts in highly phyric (>10 vol.%) basalts are very similar to those of accessory lithic fragments from subunit F in Unit II (equant to subequant dusty plagioclase, tabular plagioclase with clear core, euhedral and skeletal olivine, and euhedral and elongate orthopyroxene). Plagioclase phenocrysts sometimes appear as broken crystals. Several large plagioclases (>200 micron) exhibiting reverse and/or oscillatory zoning (Fig. 3E), implying complex magma differentiation processes such as magma mixing or crustal contamination or successive magma in-

jections in magma chamber. Olivine phenocrysts in sparsely phyric basalts are the same with those from subunit G in Unit II (subhedral and subround shape). Rims of a few rounded olivine phenocrysts are surrounded by tiny fibrous orthopyroxene, showing reaction between the olivine and host basaltic magma. Clinopyroxene and magnetite occur only as microphenocrysts (<100 micron). Clinopyroxene microphenocrysts are subhedral to anhedral and fragmentary shape. Groundmasses in Unit III show cryptocrystalline variolitic texture. They are acicular plagioclase, bladed to elongated pyroxenes, tiny rhomb to skeletal magnetite, glass and mesostasis (Fig. 3E, F).

Unit IV (subunits M–R): In contrast to Unit III, petrography of Unit IV rocks is nearly identical in each other. All the Unit IV rocks are highly vesicular (porosity >60 vol.%) scoria. They are aphyric, sparsely plagioclase phyric (<1 vol.%), and sparsely olivine-plagioclase phyric (up to 2 vol.%) basalts. Plagioclase phenocrysts are subhedral and equant to tabular shape, and some equant crystals have melt inclusions. Olivine phenocrysts are euhedral and skeletal shape and commonly contain spinel and melt inclusions. Groundmasses in Unit IV basalts are acicular plagioclase, fibrous pyroxenes, tiny magnetite, glass, and mesostasis. The grain size of groundmass plagioclase and pyroxenes in Unit IV is smaller than Unit III basalts, indicating that crystallinity of Unit IV basalts are immature compared to Unit III basalts. This fact is apparent when we compare amounts of magnetite minerals in groundmasses in reflected light (Fig. 3 F, H). Another note is that mode of glass in Unit IV is hither than that in Unit III. The higher crystallinity and higher glass mode in Unit IV would indicate that cooling speed of Unit IV magma was faster than that of Unit III magma.

Variation of density and porosity

True density, apparent density, and porosity of the Hoei air-fall deposits are plotted against the height (from the bottom of Hoei air-fall deposits)

of the FJ19 outcrop in Fig. 5. Since the rock of scoria cone (FJ55) was effused after the eruption of the Hoei air-fall deposits, its values are plotted on the top of the figure.

The true density stepwise increases with increasing height, and this variation is consistent with constituent rocks; from bottom to top, juvenile clasts are changed from dacite (Unit I) through andesite (Unit II) to basalt (Units III and IV). With increasing height, the apparent density of juvenile air-fall clasts increases from Unit I (<1.0 g/cm^3) to Units II and III (up to 2.3 g/cm^3), but decreases from Unit III to Unit IV (down to 0.6 g/cm^3). The variation of apparent density negatively correlate with porosity, as shown by a negative correlation between the apparent density (Fig. 5A) and the porosity (Fig. 5B). Porosities of accessory lithic fragments are distinctly lower (<20 vol.%) than those of the juvenile air-fall clasts (Fig. 5B). The porosity of the scoria cone (FJ55) was also low (28 vol.%), implying that vesicles evaporated from the rock before (and/or during) the production of the scoria cone.

Whole rock composition

The major and trace element contents and their variability in juvenile air-fall deposits show stepwise change upward from Unit I to Unit III (Fig. 5C–L). SiO$_2$, Na$_2$O, K$_2$O, Cs, Rb, Ba, Th, Pb, Hf and REEs increase with increasing height, whereas TiO$_2$, Fe$_2$O$_3$, MnO, MgO, Cr, Ni, Co and V decrease with increasing height (Fig. 5). While Al$_2$O$_2$, CaO, P$_2$O$_5$ and Sr increase with increasing height from bottom of Unit I to top of Unit II, they slight decrease from the top of the Unit II to Unit III. Boron and Y slightly increase with increasing height from Unit I to Unit II, but they show sudden decrease from Unit II to Unit III (e.g., Fig. 5K). Although analytical results of Nb and S contents are shown in Table 2, there contents are as low as their accuracies of XRF analysis (Table 2). Thus we cannot identify any systematic variation for these two elements, and they are not used for the following discussion. Generally, major and trace element variability decreases with increasing height from Unit I to Unit III. It is

notable that the element variability of Unit IV is narrower than that of Unit III, while element contents of Unit IV are within the compositional variations of Unit III (Fig. 5). Moreover, the scoria cone has very similar compositions with Unit IV air-fall clasts, implying that exploded magma was homogeneous from the beginning of eruption of Unit IV to the end of eruption. The wider chemical variability of Unit III and homogeneity of Unit IV are consistent with the petrological description; Unit III has variable assemblage and mode of phenocryst, while Unit IV has nearly identical petrography.

All samples of accessory lithic fragments in this study were collected from Unit II. Although all juvenile clasts of Unit II have felsic compositions (andesite and dacite), the lithic fragments are mafic basalt (Fig. 5). When we compare the compositions of the lithic fragments to those of juvenile basalts (from Units III and IV), the lithic fragments are characterized by their low concentrations of most incompatible elements (TiO$_2$, K$_2$O, Na$_2$O, P$_2$O$_5$, Rb, Ba, Nb. Pb, Zr, REEs; Table 2 and Fig. 6).

Discussion

Evaluation of fractional crystallization

Watanabe *et al.* (2006) proposed that chemical variations of juvenile clasts of Hoei eruption were explained by fractionation of the observed phenocrysts assemblages based on least squares major element modeling and successive trace element modeling. Nearly identical Nd-Sr-Pb isotope compositions of all juvenile clasts supported the fractional crystallization propose (Watanabe *et al.*, 2006). However following problems have been remained; (1) Fractional crystallization of hornblende, which is identified as phenocryst phase in dacite clasts in this study, was not considered, (2) Although clinopyroxene phenocryst is not present in andesite and dacite clasts, they used the mineral in the major element modeling, (3) Some important incompatible elements (Cs, Rb, Th, B, Pb, Y) were not evaluated in the trace element modeling. In order to solve the problems,
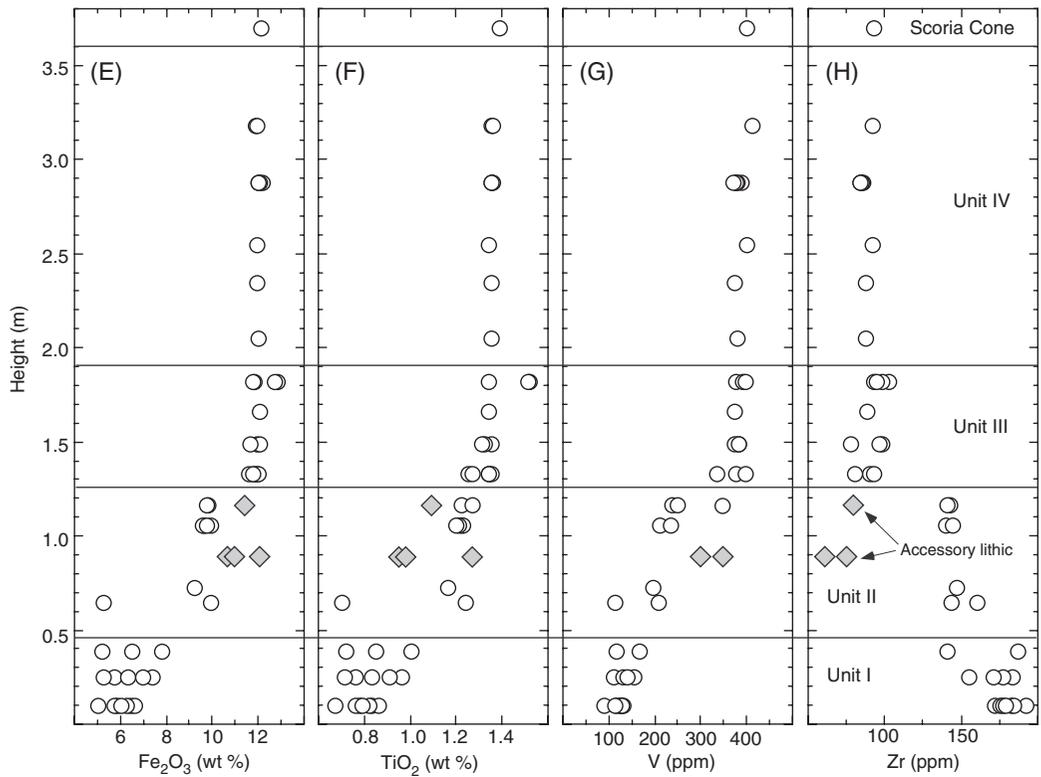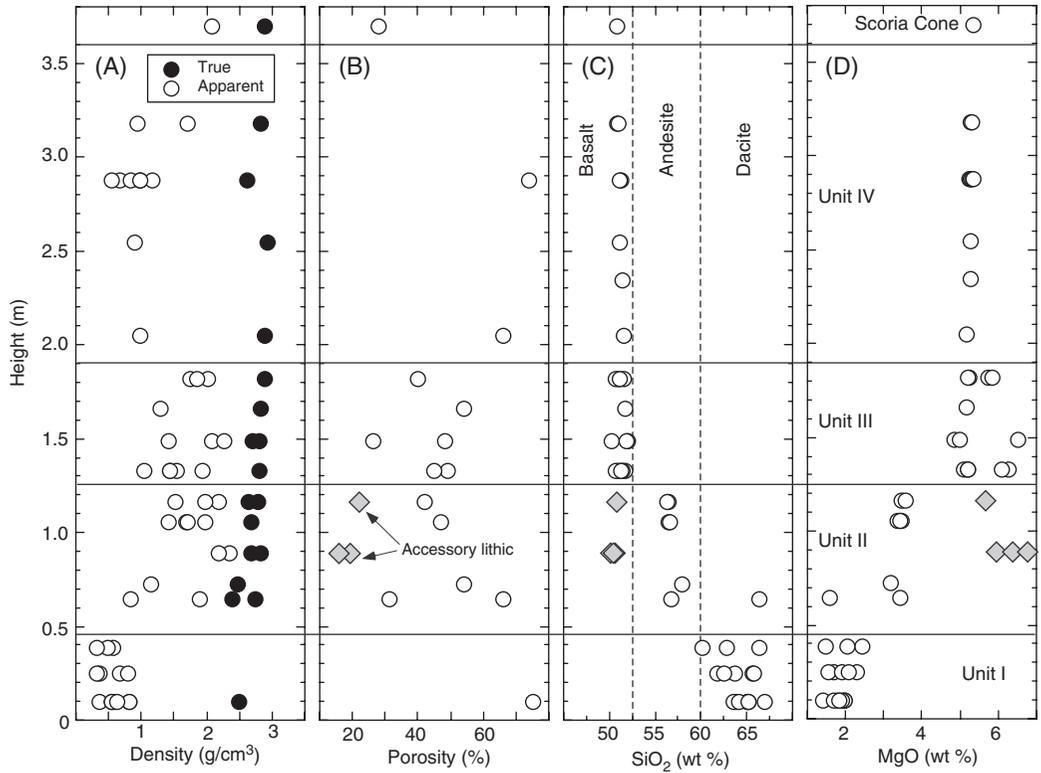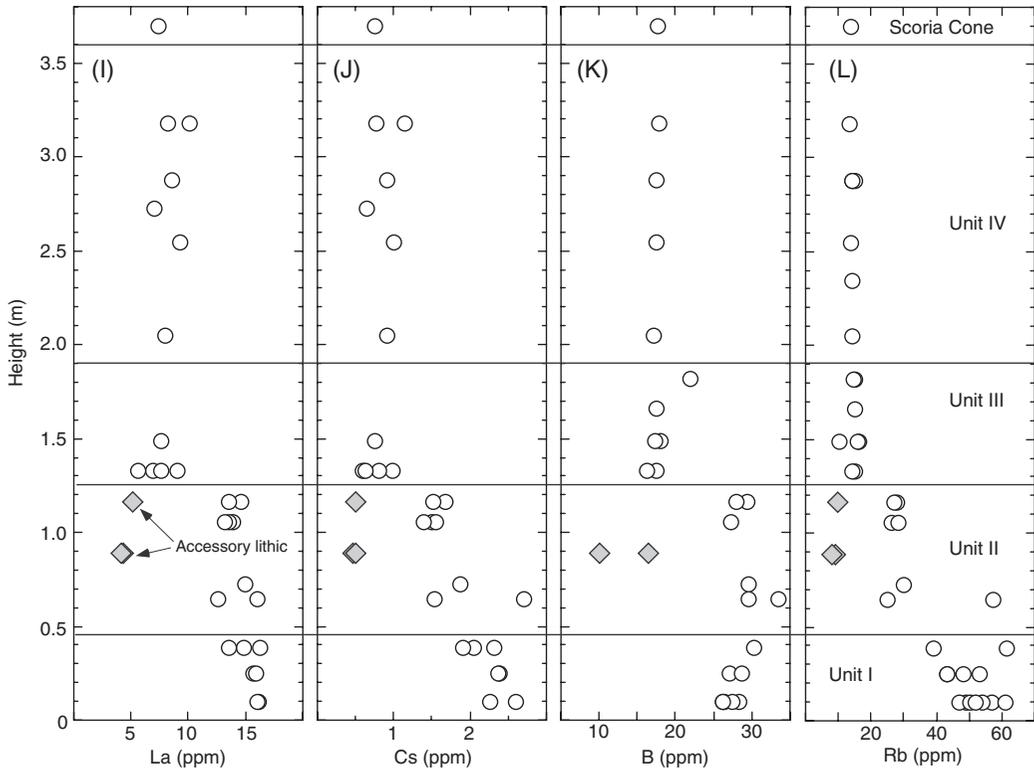
Fig. 5. Stratigraphic variations of whole-rock. (A), density; (B), porosity; (C), SiO₂ contents; (D), MgO contents; (E), Fe₂O₃ contents; (F), TiO₂ contents; (G), V contents; (H), Zr contents; (I), La contents; (J), Cs contents; (K), B contents; (L), Rb contents. Stratigraphic division follows Miyaji (1984).

we reevaluated the fractional crystallization process.

Since Watanabe *et al.* (2006) have modeled the fractional crystallization in three steps, from basalt to andesite, from andesite to dacite, and least evolved dacite to most evolved dacite, we accepted them. We selected one sample from each group as parent and/or daughter of the fractional crystallization calculation (FJ55 for basalt, FJ19-H1 for andesite, FJ19-C1 for the least evolved dacite, and FJ19-A3 for the most evolved dacite, respectively). The selected samples have similar compositions to average compositions of each group.

A least-squares mixing calculation from basalt to andesite, using whole-rock compositions reported in this study and mineral compositions reported by Watanabe *et al.* (2006) and this study (for hornblende), indicated that subtractions of

two phenocryst phases (olivine and plagioclase) and two microphenocryst phases (clinopyroxene and magnetite) from a starting basalt compositions (FJ55) produced a daughter andesite compositions (FJ19-H1). This result is nearly identical to that reported by Watanabe *et al.* (2006). On the other hand, results of least squares mixing calculations from andesite (FJ19-H1) to dacite (FJ19-C1) and from least evolved dacite (FJ19-C1) to most evolved dacite (FJ19-A3) were distinctly different from those of Watanabe *et al.* (2006). We therefore show these results in Table 3, and the high degree of fit between observed and calculated compositions are indicated by the low sum of squares of residual (0.31 and 0.33).

The least-squares mixing calculations suggest that hornblende plays important role in the fractional crystallization from andesite to most
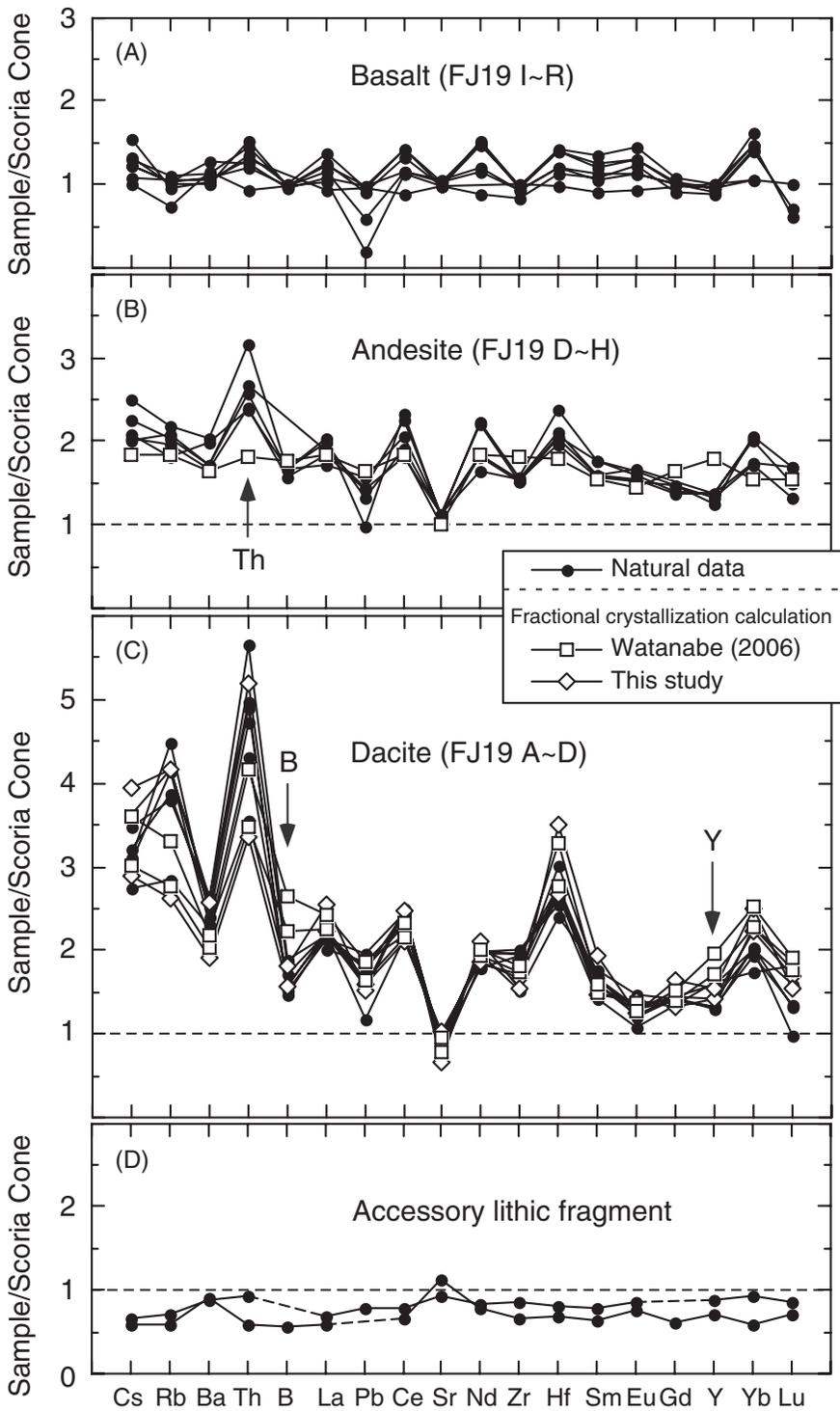
Fig. 6.   Incompatible element patterns (spiderdiagram). (A), juvenile basalt clasts (Unit III and IV); (B), juvenile andes-
ite clasts; (C), juvenile dacite clasts; (D), accessory lithic fragments. The patterns are normalized by contents of a
rock from Hoei scoria cone (FJ55). Results of fractional crystallization calculations are also shown.

evolved dacite magmas (Table 3). Instead, clinopyroxene would not be fractionated during the felsic magma evolution, and this result is consistent with the petrography that any clinopyroxene phenocrysts are not present in the felsic rocks. The major element modeling shows that other subtracted minerals are plagioclase, orthopyroxene, magnetite, and apatite (Table 3). The crystallization of hornblende from andesite and dacite magma is consistent with relatively high H_2O content in Hoei scoria (1.5–3.0 wt %; Iida et al., 2004), because of the following reason. According to the major element modeling, ~50–70 % of minerals were crystallized from basaltic magma to produce andesitic and dacitic magma. Assuming that H_2O has perfect incompatibility (D=0) to the other minerals, H_2O content in andesitic and dacitic magma is calculated to be up to 10 wt.%. At this water-rich condition,

hornblende would be crystallized when magma temperature decreased to ~900 °C (e.g., Rutherford and Devine, 2003).

The behavior of incompatible trace elements during the fractional crystallization process is further examined by using the Rayleigh fractionation equation (e.g., Shaw, 1970): $C_1/C_0 = F^{D-1}$, where, C_1 is the concentration of the element in the liquid, C_0 is the concentration of the element in the parent magma, F is the mass fraction of liquid remaining after fractional crystallization, and D is the distribution coefficient. Trace element concentrations in the starting compositions are adopted for the C_0. F is the liquid fraction obtained from the major element modeling. The D is calculated by using the mass fraction of each mineral phase estimated by the major element modeling. The distribution coefficients (Kd) compiled by McKenzie and O'Nions (1991, 1995), Piccoli and

Table 3. Fractional crystallization calculation for major elements.

	Andesite	Least evolved dacite			Most evolved dacite	
% FC[a]		24%			33%	
SSR[b]		0.31			0.33	
Mineral[c]	pl	51%		pl	64%	
prop(%)	op	8%		op	8%	
	mt	11%		mt	12%	
	ap	2%		ap	2%	
	hb	29%		hb	14%	

Sample	Parent[d] FJ19-H1	Daughter obs[e] FJ19-C1	Daughter calc[f]	Parent FJ19-C1	Daughter obs FJ19-A3	Daughter calc
SiO_2	56.67	60.95	60.78	60.95	67.34	67.22
TiO_2	1.23	1.02	1.15	1.02	0.68	0.79
Al_2O_3	17.00	16.61	16.58	16.61	15.41	15.33
$FeO*$[g]	8.97	7.20	7.06	7.20	4.57	4.46
MnO	0.18	0.15	0.14	0.15	0.10	0.11
MgO	3.47	2.46	2.51	2.46	1.41	1.40
CaO	7.16	5.74	5.59	5.74	3.90	3.80
Na_2O	3.65	3.82	4.27	3.82	3.81	4.31
K_2O	1.31	1.77	1.67	1.77	2.60	2.47
P_2O_5	0.35	0.29	0.24	0.29	0.18	0.12

[a] FC%: percentage of fractional crystallization obtained by material balance calculation.
[b] SSR: sum of squares of residual in the material balance calculation.
[c] Abbreviations used for mineral phases are the same as in Table 1, and ap is apatite.
[d] Parent composition that used for starting material of the material balance calculation.
[e] Observed composition that used for destination material of the material balance calculation.
[f] Daughter composition that calculated by the material balance calculation.
[g] Total iron expressed as FeO.

Candela (2002), and GERM website (2010) are also used to calculate the D calculation (Table 4). The trace element modeling was conducted by using two different F and D; one was reported by Watanabe *et al*. (2006), and another was reported by this study (in Tables 2 and 3). The calculation results show that the trace element modeling of this study well reproduces observed compositions, but that of Watanabe *et al*. (2006) cannot explain B and Y variations (Fig. 6). Fig. 7 also shows that trace element variations observed in the juvenile clasts are well reproduced by the Rayleigh fractionation pathways proposed by this study (solid line with arrow).

Possibility of crustal contamination

Among the incompatible trace elements, only Th variation might not be reproduced by the trace element modeling (Fig. 7); Th contents in dacite clasts are higher than the predicted values. One

possible explanation to produce the high Th content is introduction of crustal contamination. When a crustal material beneath Fuji volcano (e.g., Tertiary marine sediments and green volcanic tuffs) has distinctly higher Th than the dacite clasts, the observed composition could be explained by the crustal contamination. This fact is consistent with Os isotope data suggesting that Hoei andesite and dacite samples experienced <0.2% crustal contamination (Watanabe *et al*., 2006).

Origin of lithic fragments

Mainly two types of accessory lithic fragments are confirmed in volcanic ejecta of Hoei eruption (Tsuya, 1955; Miyaji, 1984); one is basaltic clast and another is gabbroic clast. The gabbroic clasts were proposed to be a part of magma chamber beneath Fuji volcano based on similarities in whole-rock and mineral compositions (Yasui *et*

Table 4. Solid-liquid distribution coefficient for each mineral.

Kd[a]	pl[b]	ol	op	cp	mg	ap	hb
Cs	0.025	0.00005	0.0001	0.0002	0.5	0.01	0.14
Rb	0.03	0.00018	0.0006	0.001	0.01	0.4	0.2
Ba							0.76
Th	0.05	0.0001	0.0001	0.00026	0.01	0.2	0
Nb	0.01	0.005	0.005	0.02	0.1	0.005	0.8
B	0.1	0.034	0.027	0.117	0	0.02	4[c]
La							0.17
Pb	0.36	0.0001	0.0013	0.01	0.8	0.2	0.1
Ce							0.26
Sr							0.12
Nd							0.44
Zr							0.5
Hf	0.01	0	0.01	0.22	0.2	0.8	0
Sm							0.76
Eu							0.88
Gd							0.86
Y	0.03	0.005	0.005	0.2	0.5	10	2
Yb							0.56
Lu							0.51

[a] Kd values are mainly from McKenzie and O'Nions (1991, 1993), Piccoli and Candela (2002), and the GERM website (2010). D values not shown in this table are from Watanabe et al. (2006).
[b] Abbreviations used for mineral phases are the same as in Tables 2 and 3.
[c] Exact D value of B for hornblende in andesite to dacite magma has not been reported yet. Thus we estimate the value to be 4 due to B content in hornblende (we assumed to be 100-120 ppm, because hydrous minerals have high B contents up to 200 ppm; Leeman and Sisson, 1996) and that in Fuji andesite and dacite (25-30 ppm in Table 2).
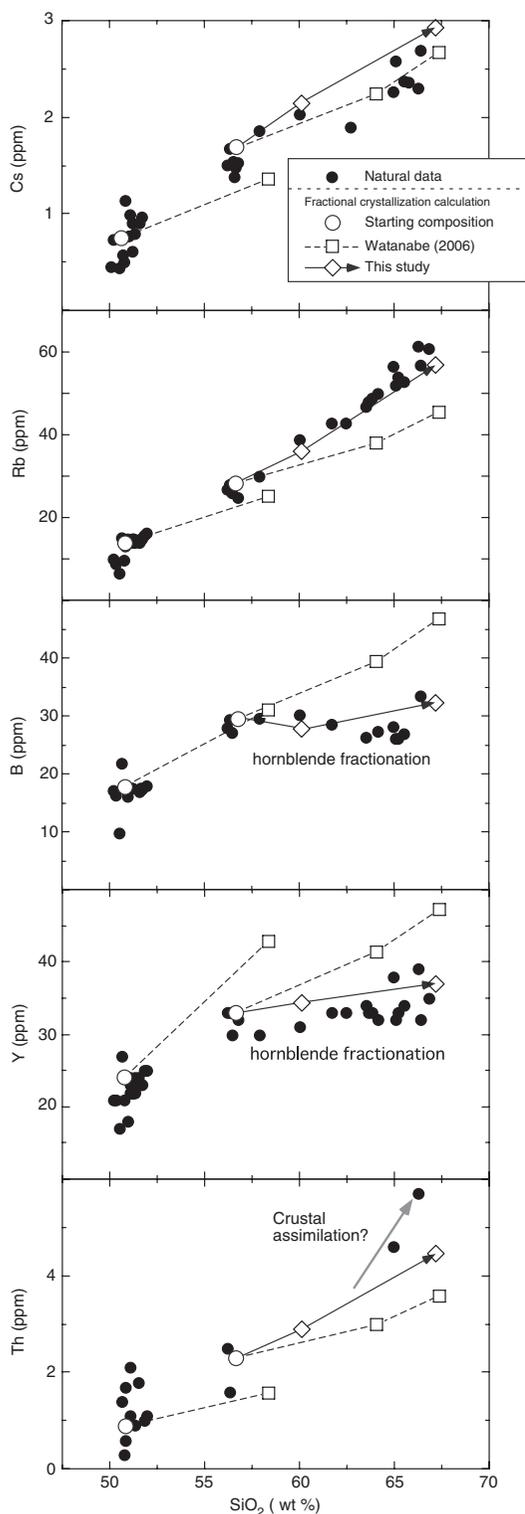
al., 1998). On the other hand, origin of basaltic clasts has not been studied in detail. We therefore examined petrological and geochemical characteristics of the basaltic lithic fragments.

Petrological difference between the lithic fragments and Hoei basaltic clasts is a presence of clinopyroxene phenocryst in lithic fragments (Table 2). The geochemical data also distinct the lithic fragments from Hoei basaltic clasts because of their low concentrations of most incompatible elements (see Whole rock composition in Results). Moreover, Rb/Y and K$_2$O/Y of the lithic fragments (Rb/Y <0.4 and K$_2$O/Y <0.03) are distinctly lower than those of Hoei basaltic clasts (Rb/Y >0.4 and K$_2$O/Y >0.03). These facts imply that a magma source of lithic fragments is different from that of Hoei magma. One plausible explanation is that lithic fragments were parts of body of Older Fuji volcano because of similarities of chemical compositions (Takahashi *et al.*, 1991, 2003; Togashi *et al.*, 1991; Togashi and Terashima, 1997; Togashi and Takahashi, 2007). When we accept the explanation, the upwelling of Hoei magma beneath the Fuji volcano exploded the lithic fragments as well as raised Hoei-san, both of which constructed body of Older Fuji Volcano.

Acknowledgements

Culture of Japan (14740307 and 21540500) to T. Sano.

References

Aizawa, K., R. Yoshimura and N. Oshiman, 2004. Splitting of the Philippine Sea plate and a magma chamber beneath Mt. Fuji, *Geophysical Research Letter*, 31, L09603, doi: 10.1029/2004GL019477.

Fujii, T, 2001. Detecting the activity of Mt. Fuji. (In Japanese) *Kagaku*, 71: 1595–1600.

Fukuoka, T., Arai, F. and Nishio, F., 1987. Correlation of tephra layers in Antarctic ice by trace element abundances and refractive indices of glass shards. *Bulletin of the Volcanological Society of Japan*, 32: 103–118.

GERM Partition coefficient (Kd) database, 2010. http://earthref.org/GERM/index.html.

Iida, A., T. Fujii and A. Yasuda, 2004. Melt inclusion study on two contrasting eruptions, the Jyogan and Hoei eruptions at Mt. Fuji. (In Japanese) *Chikyu Monthly Special Vol*. 48: 131–138.

Imai, N., S. Terashima, S. Itoh and A. Ando, 1995. 1994 complication of analytical data for minor and trace elements in seventeen GSJ geochemical reference samples, "igneous rock series", *Geostandards Newsletter*, 19: 135–213.

Ishida, M., 1992. Geometry and relative motion of the Philippine Sea plate and Pacific plate beneath the Kanto-Tokai distinct, Japan. *Journal of Geophysical Research*, 97: 489–513.

Kimura, J. and Y. Yamada, 1996. Evaluation of major and trace element XRF analyses using a flux to sample ratio of two to one glass beads. *Japanese Magazine of Mineralogical and Petrological Sciences*, 91: 62–72.

Koyaguchi, T., 1986. Mixing mechanism of mafic and felsic magmas: Origin of heterogeneous magmas, (In Japanese with English abstract) *Bulletin of the Volcanological Society of Japan*, 30: S41–S54.

Koyama, M., 1998. Reevaluation of eruptive history of Fuji volcano, Japan, mainly based on historical documents. (In Japanese with English abstract) *Bulletin of the Volcanological Society of Japan*, 43: 323–347.

Leeman, W.P. and V.B. Sisson, 1996. Geochemistry of boron and its implications for crustal and mantle processes. *In*, Grew, E.S., and L.M. Anovitz (eds.), Reviews in Mineralogy, Vol. 33, pp. 645–707.

Machida, H., 2007. Development of Fuji volcano: A review from Quaternary tephrochronology. (In Japanese with English abstract.) *In*, Aramaki, S., T. Fujii, S. Nakada, and N. Miyaji (eds.), Fuji volcano, pp. 29–44, Yamanashi Institute of Environment Sciences, Yamanashi.

Miyaji, N., 1984. Wind effect on the dispersion of the Fuji

1707 tephra. (In Japanese with English abstract) *Bulletin of the Volcanological Society of Japan*, 29: 17–30.

Miyaji, N., 1988. History of Younger Fuji Volcano. (In Japanese with English abstract) *Journal of Geological Society of Japan*, 94: 433–452.

Miyaji, N., 2007. Eruptive history, eruption rate and scale of eruptions for the Fuji volcano during the last 11,000 years. (In Japanese with English abstract) *In*, Aramaki, S., T. Fujii, S. Nakada, and N. Miyaji (eds.), Fuji volcano, pp. 79–95, Yamanashi Institute of Environment Sciences, Yamanashi.

Miyaji, N. and M. Koyama, 2007. Recent studies on the 1707 (Hoei) eruption of Fuji volcano. (In Japanese with English abstract) *In*, Aramaki, S., T. Fujii, S. Nakada, and N. Miyaji (eds.), Fuji volcano, pp. 219–231, Yamanashi Institute of Environment Sciences, Yamanashi.

McKenzie, D. and O'Nions, R.K., 1991. Partial melt distributions from inversion of rare earth element concentrations. *Journal of Petrology*, 32: 1021–1091.

McKenzie, D. and O'Nions, R.K., 1995. The source regions of ocean island basalts. *Journal of Petrology*, 36: 133–159.

Nakamichi, H., H. Watanabe and Ohminato, T., 2007. Three-dimensional velocity structures of Mount Fuji and the South Fossa Magna, central Japan. *Journal of Geophysical Research*, 112, B03310, doi: 10.1029/2005JB004161.

Nakamura, T., M. Banju, M. and J. Sato, 1986. Compositional variation within the 1707 fallout tephra from Fuji volcano. (In Japanese with English abstract) *Bulletin of the Volcanological Society of Japan*, 31: 253–264.

Piccoli, P.M. and P.A. Candela, 2002. Apatite in igneous system. *In*: Kohn, M.J., J. Rakovan, J.M. Hughes (eds.), Reviews in Mineralogy and Geochemistry, Vol. 48, pp. 255–292, Mineralogical Society of America, Washington.

Rutherford, M.J. and J.D. Devine, 2003. Magmatic conditions and magma ascent as indicated by hornblende phase equilibria and reactions in the 1995-2002 Soufriere Hill magma. *Journal of Petrology*, 44: 1433–1454.

Sano, T., 2002, Determination of major and trace element contents in igneous rocks by X-ray fluorescence spectrometer analysis (in Japanese with English abstract), *Bulletin of Fuji Tokoha University*, 2: 43–59.

Sano, T., T. Fukuoka, T. Hasenaka, C. Yonezawa and H. Matsue, 1999. Accurate and efficient determination of boron content in volcanic rocks by neutron induced prompt gamma-ray analysis, *Journal of Radioanalytical and Nuclear Chemistry*, 239: 613–617.

Sano T., T. Hasenaka, H. Sawahata and T. Fukuoka, 2006. Determination of Ti, K, Sm and Gd values in Geological Survey of Japan reference materials by prompt gamma neutron activation analysis. *Geostandards and Geoanalytical Research*, 30: 31–37.

Sasaki, T. and Y. Katsui, 1981. A new technique for measuring density of pumice using glass beads. (In Japanese) *Bulletin of the Volcanological Society of Japan*, 2: 117–118.

Shaw, D.M., 1970. Trace element fractionation during anatexis. *Geochimica et Cosmochimica Acta*, 34: 237–243.

Takada, A., Y. Ishizuka, S. Nakano, T. Yamamoto, M. Kobayashi and Y. Suzuki, 2007. Characteristics and evolution inferred from eruptive fissured of Fuji volcano, Japan. (In Japanese with English abstract.) *In*, Aramaki, S., T. Fujii, S. Nakada, and N. Miyaji (eds.), Fuji volcano, pp. 97–118, Yamanashi Institute of Environment Sciences, Yamanashi.

Takahashi, M., Y. Hasegawa, M. Tsukui, and Y. Nemoto, 1991. Evolution of magma-plumbing system beneath Fuji volcano: On the view point of whole-rock chemistry. (In Japanese with English abstract) *Bulletin of the Volcanological Society of Japan*, 36: 281–296.

Takahashi, M., M. Kominami, Y. Nemoto, Y. Hasegawa, T. Nagai, H. Tanaka, N. Nishi and M. Yasui, 2003. Whole-rock chemistry for eruptive products of Fuji volcano, central Japan: Summary of analytical data of 847 samples. (In Japanese with English abstract) *Bulletin of College of Humanities and Sciences, Nihon University*, 38: 117–166.

Terry, R.D. and G.V. Chilingar, 1955. Summary of "concerning some additional aids in studying sedimentary formations", by Shvetsov, M.S. *Journal of Sedimental Petrology*, 25: 229–234.

Togashi, S., N. Miyaji and H. Yamazaki, 1991. Fractional crystallization in a large tholeiitic magma chamber during the early stage of the Younger Fuji Volcano, Japan. (In Japanese with English abstract) *Bulletin of the Volcanological Society of Japan*, 36: 269–280.

Togashi, S. and M. Takahashi, 2007. Geochemistry of rocks form the Fuji volcano, Japan: Constraints for evolution of magmas. (In Japanese with English abstract) *In*, Aramaki, S., T. Fujii, S. Nakada, and N. Miyaji (eds.), Fuji volcano, pp. 219–231, Yamanashi Institute of Environment Sciences, Yamanashi.

Togashi, S. and S. Terashima, 1997. The behavior of gold in unaltered island arc tholeiitic rocks from Izu-Oshima, Fuji and Osoreyama volcanic areas, Japan, *Geochimica et Cosmochimica Acta*, 61: 543–554.

Tsuya, H., 1940. Geological and petrological studies of Volcano Fuji III: Geology of southwestern foot of Volcano Fuji. *Bulletin of Earthquake Research Institute*, 18: 419–445.

Tsuya, H., 1955. Geological and petrological studies of Volcano Fuji V: On the 1707 eruptions of Volcano Fuji. *Bulletin of Earthquake Research Institute*, 33: 341–384.

Tsuya, H., 1968. *Geology of Volcano Mt. Fuji*, explanatory text of geological map 1: 50,000 scale. 24 pp., Geological Survey of Japan.

Tsuya, H., 1971. *Fuji-san*, Results of the co-operative scientific survey of Mt. Fuji, Topography and geology of volcano Mt. Fuji (in Japanese with English abstract), 149pp., Fuji Kyuko Co. Ltd., Tokyo.

Ukawa, M., 2005. Deep low-frequency earthquake swarm in the mid crust beneath Mount Fuji (Japan) in 2000 and 2001. *Bulletin of Volcanology*, 67: 47–56.

Watanabe, S., E. Widow, T. Ui, N. Miyaji and A.M. Roberts, 2006. The evolution of a chemically zoned magma chamber: The 1707 eruption of Fuji volcano, Japan. *Journal of Volcanology and Geothermal Research*, 152: 1–19.

Yasui, M., S. Togashi, Y. Shimomura, S. Sakamoto, N. Miyaji, and K. Endo, 1998. Petrological features ad origin of the gabbroic fragments contained in the 1707 pyroclastic fall deposits, Fuji volcano, Japan. (In Japanese with English abstract) *Bulletin of the Volcanological Society of Japan*, 43: 43–59.

Yamamoto, T., Y. Ishizuka, and A. Takada, 2007. Surface and subsurface geology at the southwestern foot of Fuji volcano, Japan: New stratigraphy and chemical variations of the products. (In Japanese with English abstract) *In*, Aramaki, S., T. Fujii, S. Nakada, and N. Miyaji (eds.), Fuji volcano, pp. 97–118, Yamanashi Institute of Environment Sciences, Yamanashi.

Yonezawa, C., 1993. Prompt gamma-ray analysis of elements using cold and thermal reactor guided neutron beams. *Analytical Sciences*, 9: 185–186.

Yoshida, H., and N. Takahashi, 1997. Chemical behavior of major and trace elements in the Horoman mantle diapir, Hidaka belt, Hokkaido (In Japanese with English abstract), Japanese Magazine of Mineralogical and Petrological Sciences, 92: 391–409.

Yoshimoto, M., T. Fujii, T. Kaneko, A. Yoshida, and S. Nakada, 2004. Multiple magma reservoirs for the 1707 eruption of Fuji volcano, Japan. *Proceedings of Japan Academy, Ser. B*, 80: 103–106.

富士火山のマグマ分化への岩石学的制約：1707年宝永噴火のを例として

佐野貴司・福岡孝昭・石本光憲

　富士火山のマグマ分化を調べるため，西暦 1707 年に噴出した火山岩の空隙率，薄片記載，鉱物分析，全岩化学分析を行った．対象の火山岩は玄武岩，安山岩，デイサイト組成をもつ本質岩片（スコリアと軽石）および玄武岩質の類質岩片である．多くの火山岩の斑晶モードは低いが（≦3%），いくつかの安山岩質岩片と全ての類質岩片の斑晶モードは比較的高い（最大 15 %）．本質岩片の玄武岩から安山岩までの組成バリエーションは，ほぼ無水条件での斑晶鉱物の玄武岩質マグマからの分別により説明される．一方，デイサイト質岩片が角閃石斑晶を持つことと，安山岩とデイサイトの B（ホウ素）および Y 含有量がほぼ同量であることを考え合わせると，安山岩からデイサイトを形成した分別結晶作用は含水条件であったと推定される．更にデイサイト岩片中の Th 含有量が高い事実は，僅かな地殻物質の混染作用があったことで説明される．類質岩片に関しては，Rb/Y，K_2O/Y 比が低く，液相濃集元素（Ti, Na, K, P, Rb, Ba, Nb, Pb, Zr, REEs）含有量が低いため，本質岩片とは異なるマグマソースを持つと考えられる．